# Pyk2 Overexpression in Postsynaptic Neurons Blocks $A\beta_{1-42}$-induced Synaptotoxicity in a Microfluidic Co-Culture Model

Devrim Kilinc[a]*, Anaïs-Camille Vreulx[a], Tiago Mendes[a], Amandine Flaig[a], Diego Marques-Coelho[b, c], Maxime Verschoore[a], Florie Demiautte[a], Philippe Amouyel[a], Neuro-CEB Brain Bank, Fanny Eysert[a], Pierre Dourlen[a], Julien Chapuis[a], Marcos Romualdo Costa[a, b], Nicolas Malmanche[a], Frederic Checler[d] and Jean-Charles Lambert[a]*

[a] Université de Lille, Institut Pasteur de Lille, CHU Lille, INSERM U1167, LabEx DISTALZ, 1 rue du Prof Calmette, BP245, Lille 59019 France
[b] Brain Institute, Federal University of Rio Grande do Norte, Av. Nascimento de Castro 2155 Natal, Brazil
[c] Bioinformatics Multidisciplinary Environment (BioME), Federal University of Rio Grande do Norte, Av. Nascimento de Castro 2155 Natal, Brazil
[d] CNRS UMR7275 Laboratory of Excellence "Distalz", IPMC, Université Côte d'Azur, Inserm. 660 Route des Lucioles, Sophia-Antipolis, Valbonne 06560 France
* Corresponding authors: devrim.kilinc@pasteur-lille.fr; jean-charles.lambert@pasteur-lille.fr

**Recent meta-analyses of genome-wide association studies identified a number of genetic risk factors of Alzheimer's disease (AD); however, little is known about the mechanisms by which they contribute to the pathological process. As synapse loss is observed at the earliest stage of AD, deciphering the impact of AD risk genes on synapse formation and maintenance is of great interest. In this paper, we report a microfluidic co-culture device that physically isolates synapses from pre- and postsynaptic neurons and chronically exposes them to toxic amyloid-beta (Aβ) peptides secreted by model cell lines overexpressing wild-type or mutated (V717I) amyloid precursor protein (APP). Co-culture with cells overexpressing mutated APP exposed the synapses of primary hippocampal neurons to $A\beta_{1-42}$ molecules at nanomolar concentrations and induced a significant decrease in synaptic connectivity, as evidenced by distance-based assignment of postsynaptic puncta to presynaptic puncta. Treating the cells with antibodies that target different forms of Aβ suggested that low molecular weight oligomers are the likely culprit. As proof of concept, we demonstrate that overexpression of Pyk2 –an AD risk gene involved in synaptic plasticity and shown to decrease in AD brains at gene expression and protein levels– selectively in postsynaptic neurons is protective against $A\beta_{1-42}$-induced synaptotoxicity. In summary, our lab-on-a-chip device provides a physiologically-relevant model of AD-related synaptotoxicity, optimal for assessing the impact of risk genes in pre- and postsynaptic compartments.**

## Introduction

Alzheimer's disease (AD), the most common neurodegenerative disorder worldwide, is characterized by two types of brain lesions: (i) neurofibrillary degeneration due to the intracellular aggregation of abnormally hyperphosphorylated tau protein and (ii) amyloid plaques resulting from the extracellular accumulation of amyloid beta (Aβ) peptides (1). Aβ peptides are generated by the cleavage of the transmembrane amyloid precursor protein (APP) and can have different residue lengths (2). The discovery of mutations in the APP, PS1 and PS2 genes (coding for APP and presenilins 1 and 2) causing early-onset, autosomal-dominant forms of AD has profoundly influenced our understanding of the disease, and has placed Aβ peptides at the center of the pathophysiological process. According to the "amyloid cascade hypothesis", the accumulation of Aβ

peptides is the triggering toxic condition that induces the development of neurofibrillary degeneration and thus neuronal death (3).

$A\beta_{1-42}$ species have been the principal focus of research (4) since $A\beta_{1-42}$ is more prone to oligomerize (5, 6) and oligomers of $A\beta_{1-42}$ are more toxic than its monomeric or fibrillary forms, and other Aβ species (7-9). Oligomeric $A\beta_{1-42}$ is in a dynamic equilibrium with the monomeric forms and fibrils, and has been proposed to be the main promoter of amyloid plaques (10). Although the central role of the Aβ peptide burden as initially enunciated in this hypothesis is strongly debated, several lines of evidence indicate that Aβ peptides are still a key actor of the disease at least *via* their oligomeric forms. In particular, the Aβ oligomer toxicity has been linked with synapse dysregulation and loss (11).

Synapse loss is a major pathological correlate of cognitive deficits in AD (12) and is observed at the earliest stage of the disease (13). Several mechanisms have been proposed to explain Aβ-induced synaptotoxicity: (i) membrane-disrupting activity at high concentrations (14); (ii) deleterious pruning of synapses by microglia activation (15); (iii) direct interaction of oligomeric forms with postsynaptic receptors, such as ionotrophic or metabotropic glutamate receptors (16, 17). In addition, the new genetic landscape of AD, resulting from the advent of the genome wide association studies (GWAS) (18, 19), highlights synaptic (dys)regulation: several among the dozens of genes/loci identified to be associated with AD risk, *e.g.*, *BIN1*, *CD2AP*, *FERMT2* and *PTK2B*, have been shown to modulate synaptic functions in the physio- and/or pathophysiological contexts (20-24). As a result, we recently proposed a genetically-driven synaptic failure hypothesis, based on the genetic and post-GWAS data (25). In this context, Aβ toxicity is one of the elements involved in synapse failure and it may be driven by specific AD genetic risk factors.

However, assessing such an hypothesis requires a number of considerations to be taken into account: (i) most *in vitro* models of Aβ toxicity use synthetic Aβ oligomers at non-physiological concentrations, even though synthetic fibrils are structurally different from Aβ fibrils obtained from AD brains (26); (ii) only a few of the GWAS-defined genes have been analyzed in a (physiological and/or pathophysiological) synaptic context; (iii) GWAS-defined genes may have different effects when expressed in the pre- or postsynaptic neurons. For example, proline-rich tyrosine kinase 2 (Pyk2), product of AD risk gene *PTK2B*, directly interacts with postsynaptic scaffold proteins (27), regulates dendritic spine morphology (20), and is involved in synaptic plasticity through regulating postsynaptic NMDA receptors *via* activation of Src (28). Recent studies based on AD mouse models linked Pyk2's effects to amyloid pathology, but reported contradictory data on whether lack of Pyk2 was detrimental or protective (23, 29).

With this background, we have developed a microfluidic co-culture device, based on existing tricompartment designs that physically isolate synapses and provide exclusive access to pre- and postsynaptic neurons (30, 31). This device permits not only the induction of synaptotoxicity *via* physiologically-relevant concentrations of Aβ molecules secreted by cells stably overexpressing human APP, but also the analysis of synaptic density as a function of over- or underexpression of genetic risk factors in pre- and/or postsynaptic neurons. In this paper, we characterized Aβ-induced synaptotoxicity in primary neurons upon co-culture with cells overexpressing mutated APP and assessed the impact of Pky2 overexpression in postsynaptic neurons, as a proof of concept.

# Experimental

### Oligimerization of synthetic Aβ peptides

Aβ peptides were oligomerized according to established protocols (4, 32) with minor modifications. The inactive control peptide ($A\beta_{42-1}$; Abcam; Cambridge, UK) has the same composition as the $A\beta_{1-42}$ peptide (California Peptide Research; Napa, CA) but with an inverted amino-acid sequence, and has been widely used as control for oligomeric $A\beta_{1-42}$ since it is also prone to oligomerization (33-35). $A\beta_{1-42}$ and ICP were treated with hexafluoroisopropanol (Sigma-Aldrich, Saint Louis, MO) to maintain the oligomeric structure and to reduce fibril formation (4), according to manufacturer's instructions. The peptides were resuspended in 1 ml hexafluoroisopropanol and incubated for 1 h at RT, with occasional moderate vortexing, followed by

sonication in water bath (Branson; Emerson Electric; St. Louis, MO) for 10 min. The solution was aliquoted into microcentrifuge tubes, let to evaporate in a chemical fume hood, dried with SpeedVac system (Thermo Fisher Scientific, Waltham, MA) for 30 min, and stored as desiccated peptide at -80°C. To produce oligomers, lyophilized, hexafluoroisopropanol-treated aliquots of both peptides were resuspended in DMSO to reach 5 mM, mixed by pipetting, sonicated in water bath for 10 min, diluted to 100 µM in ice-cold D-PBS, followed by 30 s vortexing and 1 h incubation at 25°C. The solutions were aliquoted into microcentrifuge tubes and stored at -20°C for up to 4 weeks. Before adding to neurons, oligomeric peptide stocks were thawed, serial diluted to 100 nM in 2 % DMSO in PBS. $A\beta_{1-42}$ concentrations up to 1 µM are considered non-lethal (36, 37).

**Microfluidic device design and fabrication**

The microfluidic co-culture device was designed based on a previous tricompartmental neuron culture device (38). The device consists of a 300 µm wide, 7.4 mm long central channel flanked by two 750 µm wide, 3.6 mm long side channels. All three channels are *ca*. 100 µm high. The left side channel (termed presynaptic) and the central channel (termed synaptic) are interconnected *via* 4 µm high, 450 µm long parallel microchannels that narrow from an entry width of 10 µm to an exit width of 3 µm. The right side channel (termed postsynaptic) and the synaptic chamber are also interconnected *via* parallel microchannels with identical dimensions, except that they were 75 µm long. One end of the synaptic chamber bifurcates into two branches, one of which terminates in a triangular shape. This terminus is connected to a diamond-shaped co-culture chamber (based on a previous design) (39) *via* 4 µm high, 10 µm wide, and 100 µm long parallel microchannels.

Master patterns were fabricated at the IEMN (Lille, France) *via* two-step photolithography (40). Ca. 4 mm high polydimethysiloxane (PDMS) pads were replica molded. Access wells were punched at the termini of the central channel and the co-culture chamber, and of the side channels using 3 mm and 4 mm biopsy punches (Harris Unicore), respectively. The devices were permanently bonded to 24 mm × 50 mm glass coverslips (Menzel) *via* $O_2$ plasma (Diener, Ebhausen, Germany). Prior to cell culture, the devices were sterilized under UV light (Light Progress, Anghiari, Italy) for 30min, treated with 0.1 mg/mL PLL overnight, and rinsed with PBS.

**Primary neuron culture**

Culture media and supplements were from Thermo Fisher, unless mentioned otherwise. Primary neurons were obtained from P0 rats, according to previously described procedures (41). Briefly, cortices and hippocampi were isolated from new-born rats, washed with ice-cold dissection medium (HBSS supplemented with HEPES, sodium pyruvate, and penicillin/streptomycin), and trypsinized (2.5%; at 37°C for 10 min). Trypsin was inactivated with dissociation medium –MEM supplemented with fetal bovine serum (FBS), Glutamax, D-glucose (Sigma), MEM vitamins, and Pen/Strep– followed by DNase (5 mg/ml; Sigma) incubation for 1 min and wash with dissection medium. Media was replaced by dissociation medium and tissue was triturated with a fire-polished cotton-plugged Pasteur pipette to obtain a homogenous cell suspension, followed by centrifugation (200× *g* for 5 min). Cells were resuspended in culture medium (Neurobasal A supplemented with Glutamax and $B_{27}$ neural supplement with antioxidants), counted, and plated at a density of 100,000 cells/cm$^2$ in 6- and 24-well plates for immunoblots and in 10 cm Petri dishes for synaptosome extraction. Plates were pre-coated with 0.1 mg/mL poly-l-lysine (Sigma) in 0.1M borate buffer (0.31% boric acid, 0.475% sodium tetraborate, pH = 8.5; Sigma) overnight at 37°C and rinsed thoroughly with water. Alternatively, cells were plated in pre-coated 384-well plates at 50,000 cells/cm² (*ca*. 4,000 cells/well) and in microfluidic devices at a density of *ca*. $8\times10^5$ cells/cm$^2$. After 20-24 h, culture media was replaced with supplemented Neurobasal A medium. 0.1% ethylenediaminetetraacetic acid (EDTA; in $H_2O$) was added to the Petri dishes containing microfluidic devices to minimize evaporation. Cultures were maintained in a tissue culture incubator (Panasonic; Osaka, Japan) at 37°C and 5% $CO_2$.

**Immunoblotting**

Neurons were harvested in minimum volume of 200 µl/well in 6-well plates, in ice-cold lysis buffer as described earlier (42). Lysates were mixed with 4× LDS sample buffer (Novex; Thermo Fisher) and 10× reducing agent (Novex), sonicated, and boiled at 95°C for 10 min. Samples were loaded at maximum volume into 1.5 mm, 10-well, 4-12% Bis-Tris pre-cast NuPage gels (Novex), along with 5 µl MW marker (Novex Sharp pre-stained protein standard, Thermo Fisher). The gel was run with 2-(N-morpholino)ethanesulfonic acid (MES) running buffer at 200 V for 45 min and transferred to 0.22 µm nitrocellulose membranes using the Trans-Blot Turbo transfer system (BioRad, Hercules, CA) using mixed MW method at 1.3 A and 25 V for 7 min. Membranes were blocked in TNT (0.05% Tween 20, 20 mM Tris-Base, 150 mM NaCl, pH = 8.0) containing 5% non-fat dry milk for 1 h at RT and washed 3× in TNT. Membranes were incubated with the following primary antibodies in SuperBlock T20 blocking buffer (Thermo Scientific) at 4°C overnight and washed 3× in TNT: rabbit anti-phospho-PTK2B (Cell Signaling Technology 3291; 1/1,000; Danvers, MA), rabbit anti-PTK2B (Sigma P3902; 1/1,000), and mouse anti-β-actin (Sigma A1978; 1/5,000). Membranes were then incubated with horseradish peroxidase (HRP)-conjugated secondary antibodies (HRP-anti-Mouse and HRP-anti-rabbit; 1:5,000; Jackson ImmunoResearch, West Grove, PA) in TNT containing 5% non-fat dry milk for 1 h at RT and washed 3× in TNT. The membrane was revealed through chemiluminescence (Luminata Classico, EMD Merck Millipore) and imaged with Amersham Imager 600 (GE Healthcare, Mississauga, Canada). The images were quantified with ImageQuantTL Software (GE Healthcare).

**Culture of CHO cells and analysis of their media**

CHO cell lines (CHO-pcDNA4, -APP$^{WT}$ and -APP$^{LDN}$) were maintained according to previously described procedures (43). Cells were grown in CHO growth medium: DMEM/Ham's F-12 1:1 medium, supplemented with 10% heat-inactivated FBS, 0.2% Pen/Strep, 2% HT supplement, and 300 µM Proline (Sigma). To stimulate Aβ production, the growth medium was replaced with CHO-NBA medium: phenol red-free Neurobasal A (Gibco) supplemented with 0.2% Pen/Strep, 2% HT supplement, and 300 µM Proline.

For media collection, cells were grown in 10 cm Petri dishes or in 6-well plates until they reached 80% confluence, at which point the maintenance medium was rinsed with PBS and replaced with the stimulation medium. After 48 h of stimulation, the medium was collected into 15 mL Falcon tubes and centrifuged at 4,000× *g* and 4°C for 10 min to remove the debris. The supernatant was loaded into a 3 kDa spin column (Amicon Ultra; Merck), equilibrated with Neurobasal (without serum or Phenol Red) at 4,000× *g* and 4°C for 10 min, and concentrated at 4,000× *g* and 4°C for 1 h. Western blotting of conditioned media was performed as described with the following exceptions: the transferred membrane was boiled for 5 min in PBS and Luminata Crescendo (Millipore) was used as the HRP substrate. Anti-A$\beta_{1\text{-}42}$ (clone 6E10; 1:1000; Sigma) was used as primary antibody.

**Exposure of neurons to conditioned media**

Total protein concentration in the conditioned media collected from different CHO cell lines (CHO-pcDNA4, -APP$^{WT}$ and -APP$^{LDN}$) was assessed using the Pierce BCA Protein Assay Kit (Thermo Fisher) and adjusted to 100 µg/µL with supplemented CHO-NBA medium. 10 µL of conditioned media (per well) was added to primary neuronal cultures grown in 384-well plates (containing 40 µL of culture medium per well) at DIV14, DIV18, DIV19, DIV20, and DIV21 (6 h prior to media collection). Media from these wells (8 wells per condition) were collected into a new 384-well plate prior to quantification of Aβ peptides.

**Co-culture of neurons with CHO cells**

CHO cells were seeded in the co-culture chamber at a density of *ca.* $1.3\times10^5$ cells/cm$^2$ and maintained in a tissue culture incubator (5% $CO_2$; 37°C) in CHO medium. On the day of primary neuron culture, the medium was replaced with CHO-NBA medium supplemented with 1% Glutamax and 2% $B_{27}$ neural supplement with antioxidants. Primary neurons were seeded in the pre- and postsynaptic chambers. At DIV1, the medium in all wells was replaced with fresh supplemented CHO-NBA medium. Every 3-4 days, the medium in the

access wells of the co-culture chamber was replaced with fresh medium, whereas the medium in other wells were only topped up with fresh medium.

**Lentiviral transductions**

At DIV7, neurons cultured in the postsynaptic chamber were transducted with lentiviruses according to established methods.(41) To avoid transduction of CHO cells and the neurons in the presynaptic chamber, a hydrostatic pressure gradient was formed across the microchannels separating synaptic and postsynaptic chambers. The following lentiviruses were used for transduction: Mission shRNA vectors (Sigma) pLenti6/Ubc/v5-DEST (Invitrogen, Carlsbad, CA) empty (Mock) or including human PTK2B cDNA sequences, synthesized *via* the GeneArt service (Thermo Fisher). LifeAct-Ruby (pLenti.PGK.LifeAct-Ruby.W; RRID: Addgene_51009) and LifeAct-GFP (pLenti.PGK.LifeAct-GFP.W; RRID: Addgene_51010) were kind gifts from Rusty Lansford. Viral transduction was performed at multiplicity of infection (MOI) of 4. Constructs were diluted in pre-warmed, supplemented CHO-NBA medium containing 2 µg/mL (5×) Polybrene (hexadimethrine bromide; Sigma). Media from pre- and postsynaptic wells were collected in a common tube. 25 µL, 15 µL, and 20 µL of the collected media were returned to each presynaptic, synaptic, and postsynaptic well, respectively. 10 µL of virus suspension was added to one of the postsynaptic wells. Neurons were incubated with viral particles for 6 h before the wells were topped up with the remainder of the collected media. Co-cultures were maintained as described earlier.

**Alpha-LISA measurements**

Alpha-LISA is a highly sensitive, quantitative assay based on biotinylated antibody bound to streptavidin-coated donor beads and antibody-conjugated acceptor beads. In the presence of the analyte, the beads come into close proximity such that the excitation of the donor beads triggers a cascade of energy transfer in the acceptor beads, resulting in a sharp peak of light emission at 615 nm. We used Alpha-LISA kits specific to human $A\beta_{1\text{-}X}$ and $A\beta_{1\text{-}42}$ (AL288C and AL276C, respectively; PerkinElmer, Waltham, MA) to measure the amount of $A\beta_{1\text{-}X}$ and $A\beta_{1\text{-}42}$ in culture media. The human Aβ analyte standard was diluted in CHO-NBA medium. For the assay, we first added 5 µL of cell culture supernatant or standard solution into an Optiplate-96 microplate (PerkinElmer). We then added 5 µL of 10× mixture including acceptor beads and biotinylated antibody. Following incubation at RT for 60 min, we added 40 µL of 1.25× donor beads and incubated at RT for 60 min. We measured the fluorescence using an EnVision-Alpha Reader (PerkinElmer) at 680 nm excitation and 615 nm emission wavelengths. In experiments where conditioned media was added to primary neurons in 384-well plates, 2 µL of collected media was transferred to an Optiplate-384 (PerkinElmer) and Alpha-LISA was performed using reduced volumes: 2 µL of sample or standard, 2 µL of acceptor beads and biotinylated antibody mix, and 16 µL of donor beads.

**ELISA measurements**

The sandwich ELISA was performed according to the manufacturer's protocol. We used microtiter plates pre-coated with anti-human $A\beta_{35\text{-}40}$ antibody (clone 1A10; RE59781, IBL) and anti-human $A\beta_{38\text{-}42}$ (clone 1C3; RE59721, IBL) to detect $A\beta_{1\text{-}40}$ and $A\beta_{X\text{-}42}$, respectively. Plates were incubated overnight at 4°C with 100 µL cell culture supernatant or with standards. The bound antigen was detected by incubating the wells with 100 µL of 30× mixture containing the HRP-conjugated anti-human Aβ antibodies (clone 82E1 for $A\beta_{1\text{-}40}$ and clone 12B2 for $A\beta_{X\text{-}42}$) for 60 min at 4°C. Signal was revealed by incubating with the TMB substrate for 30 min at RT in the dark and stopping the enzymatic reaction with the TMB stop solution containing 1N $H_2SO_4$. Signal intensity was read immediately at 405 nm *via* a microplate reader (PowerWave XS2, BioTek Instruments, Winooski, VT).

**Immunocytochemistry and microscopy**

Co-cultures were fixed at DIV14 in PBS containing 4% paraformaldehyde for 20 min at RT and permeabilized with 0.3% (v/v) Triton X-100 in PBS for 5 min. After blocking in 5% (w/v) normal donkey

serum, samples were incubated overnight at 4°C with the following antibodies: anti-MAP2 (188011; Synaptic Systems, Göttingen, Germany); anti-Homer (160006; Synaptic Systems) and anti-PYK2 phospho-Y402 (ab4800; Abcam, Cambridge, UK). Cells were rinsed with PBS and incubated with the following secondary antibodies for 2 h at RT: Dylight 405 Donkey anti-mouse (715-475-151; Jackson); AlexaFluor 647 donkey anti-rabbit (711-605-152; Jackson) and AlexaFluor 594 Donkey anti-chicken (703-585-155; Jackson). Cells were rinsed with PBS and incubated with mouse monoclonal anti-Synaptophysin 1 pre-labeled with Oyster 488 (101011C2; Synaptic Systems) for 2 h at RT. Cells were rinsed with PBS and microfluidic devices were topped with 90% glycerol.

Samples were imaged with a LSM 880 confocal microscope (Zeiss, Oberkochen, Germany) equipped with a 63× 1.4 NA objective. Images were acquired at zoom 2 in *z*-stacks of 0.5 µm interval. Typically, 4 images were acquired per device from the synapse chamber near the postsynaptic chamber such the image contains multiple dendrites. Images were deconvoluted using AutoQuantX3 software (BitPlane, Zurich, Switzerland) for synaptic connectivity analysis.

In a subset of experiments, neurons were plated only in the presynaptic chamber, only in the postsynaptic chamber, or only in the synaptic chamber. Neurons were fixed and immunostained at DIV14 as described to reveal nuclei, GFAP (ABD95; Millipore) and β3-tubulin (MAB1637, Millipore). All chambers were imaged using a Zeiss AxioObserver Z1 epifluorescense microscope equipped with a Prime 95B Scientific CMOS (Photometrics, Tucson, AZ) camera and 32× objective. The integrated density (pixel values × area) of the β3-tubulin signal was quantified in all chambers, at a distance between 50 and 200 µm from the entries and exits of the microchannels. Neurite penetration rates for short and long microchannels (in the forward and reverse directions) were estimated by taking the ratio of the β3-tubulin integrated density signals obtained from the emitting and receiving chambers. The ratio between the penetration rates between forward and reverse directions was defined as the directionality ratio.

**Quantification of synapse integrity**

We developed an image analysis workflow based on image segmentation using Imaris software (BitPlane) and assignment of postsynaptic signals to the nearest presynaptic signal using a custom Matlab (Mathworks; Natick, MA) code. Briefly, signals obtained for pre- and postsynaptic structures were first segmented into distinct volumes using the surfaces function of Imaris in the batch mode that permits the same parameters to be applied to all images (Fig. S1A-S1D). Postsynaptic spots were then assigned to the nearest presynaptic spot (according to the distance between centers of mass) within a predefined cut-off distance (Fig. S1E). We empirically determined the cut-off distance by testing a range on a large set of control cultures (Fig. S1F-S1G). The average number and distance of such assignments and the fraction of pre- and postsynaptic signals without any assignments were used as output parameters. Note that a small fraction of control samples for CHO-APP$^{WT}$ and CHO-APP$^{LDN}$ co-cultures (2 devices each) do overlap in the data reported.

**Analysis of phospo-Pyk2 signals relative to synapses**

We extended the image analysis workflow to analyze the positions of phospho-Pyk2 (Tyr402) (p-Pyk2) puncta relative to the positions of identified synapses. Postsynaptic spots were first assigned to the nearest presynaptic spot as described. For each postsynaptic-to-presynaptic assignment, or "synapse", we defined the midpoint as being equidistant to pre- and postsynaptic puncta. We next defined pre- and postsynaptic zones, by spanning two right circular cones with 45° polar angle where the midpoint is the apex. We then associated p-Pyk2 puncta with the nearest "synapse" as long as it was within a pre-defined cut-off distance from the midpoint and categorized these associations as presynaptic, postsynaptic, or other (neither pre- nor postsynaptic). We then calculated the average number of p-Pyk2 puncta associated with each "synapse".

**Synaptosome extraction**

To verify the presence of proteins at the synaptic level we did a subcellular fractionation as previously described (44). Briefly, cortical neurons were cultured in 10 cm Petri dishes as described (3.5-4.0 × $10^7$

neurons per condition). At DIV13, neurons were exposed to CHO-APP$^{WT}$ or CHO-APP$^{LDN}$ media for 18 h (final $A\beta_{1-X}$ concentration: 40 nM). At the end of this treatment, neurons were lysed, reconstituted in a solution (0.32 M sucrose and 10 mM HEPES, pH = 7.4), and centrifuged at 1,000× *g* for 10 min to remove nuclei and debris. The supernatant was centrifuged at 12,000× *g* for 20 min to remove the cytosolic fraction. The pellet was reconstituted in a second solution (4 mM HEPES, 1 mM EDTA, pH = 7.4) and was centrifuged 2× at 12,000× *g* for 20 min. The new pellet was reconstituted in a third solution (20 mM HEPES, 100 mM NaCl, 0.5% Triton X-100, pH = 7.2) for 1 h at 4°C and centrifuged at 12,000× *g* for 20 min. The supernatant collected corresponds to the non-postsynaptic density (PSD) fraction (Triton-soluble). The remaining pellet was reconstituted in a fourth solution (20 mM HEPES, 0.15 mM NaCl, 1% Triton X-100, 1% deoxycholicacid, 1% SDS, pH = 7.5) for 1 h at 4°C and was centrifuged at 10,000× *g* for 15 min to obtain a supernatant containing the PSD fraction (Triton-insoluble). The fractions obtained were then analyzed by WB.

**Analysis of gene expression alterations in human brain samples**

RNA sequencing (RNAseq) data from the Mount Sinai/JJ Peters VA Medical Center Brain Bank (MSBB) (45), the ROSMAP database (46), and the Mayo Clinic whole genome and transcriptome data (47) were downloaded from AMP-AD Knowledge Portal (48) according to the terms and conditions concerning the use of the data. Data were aligned using pseudoaligner Kallisto version 0.43.1 (49) using a pre-built index to align fastq files. Differential gene expression analysis was performed using DESeq2 (50). First, a DESeq2 object was created using *DESeqDataSetFromTximport* function and rows with sum of all counts less than 10 were filtered out. Next, *DESeq* function was used with default parameters. Temporal cortex was analyzed in the Mayo Clinic dataset (82 AD cases and 78 healthy controls). Dorsolateral prefrontal cortex was analyzed in the ROSMAP dataset (222 AD cases and 201 controls). The following brain areas were analyzed in the MSBB dataset: Brodmann area (BA) 10, which corresponds to the anterior prefrontal cortex (105 AD cases and 71 controls); BA 22, which is part of the Wernicke's area in the superior temporal gyrus (98 AD cases and 61 controls); BA 36, which corresponds to the lateral perirhinal cortex (88 AD cases and 64 controls); and BA 44, which corresponds to the inferior frontal gyrus (90 AD cases and 63 controls).

**Analysis of neuropathological human sample cohort**

The brain samples were collected through a brain donation program dedicated to neurodegenerative dementias coordinated by the NeuroCEB Brain Bank Network. The informed consent for post-mortem examination and research studies was signed by the legal representative of each patient in patient's name, as allowed by the French law and approved by the local ethics committee and the brain bank has been officially authorized to provide samples to scientists (agreement AC-2013-1887). All procedures performed in this study involving human participants were in accordance with the ethical standards of the institutional research committees and with the 1964 Helsinki declaration. The brain banks fulfill criteria from the French Law on biological resources including informed consent, ethics review committee and data protection (article L1243-4 du Code de la Santé publique, August 2007). The Neuro-CEB brain bank (BioResource Research Impact Factor number BB-0033-00011) has been declared to the Ministry of Research and Higher Education, as required by French law.

Assessment of AD-related neurofibrillary pathology (Braak stage) was performed according to published procedures (51) by analyzing post-mortem brain tissue samples of 27 individuals (Table S1) *via* immunohistochemistry using AT8 antibody, which detects hyperphosphorylated Tau (52). Lysis buffer containing, trizma-base 20 mM; NaCl 150 mM; cOmplete Protease Inhibitor Cocktail 1X and 1% triton, was added to single pieces of whole brain tissue (~100 mg) at a ratio of 5 µL per 1 mg of tissue. Brain samples were homogenized by beads beating using a precellys soft tissue CK14 2 mL (3×30 s at 6,500 rpm). The lysate was then centrifuged at 4,000 rpm for 15 min at 4°C. 50 µL from the supernatant was used for analysis. Protein quantification was performed using BCA protein assay. Total proteins (40 µg/lane) were separated on 4-12% Bis–Tris-polyacrylamide gel electrophoresis (NuPAGE; Thermo Scientific) under

reducing conditions and subsequently blotted onto nitrocellulose membranes using iBlot 2 Dry Blotting System (Biorad). Primary antibodies against phospho-Pyk2 Tyr 402 (1:1000; Cell Signalling, cat. no. 3291), total Pyk2 (1:1000; Sigma, cat. no. P3902) and β-actin (1:5000; Abcam, cat. no. ab8226) were used for immunoblotting. After incubation with the appropriate HRP-conjugated secondary antibodies, the protein bands were detected using ImageJ. Samples outside of 3× median absolute deviations were deemed outliers and were excluded from the analysis.

## Results

### Microfluidic co-culture device to expose hippocampal synapses to synthetic or cell secreted Aβ oligomers

With the goal to better mimic AD *in vitro*, we developed a microfluidic device that permits synapse formation between two sets of neurons cultured in distinct chambers. Based on a previous design, our device consists of three distinct chambers, interconnected *via* parallel microchannels that constrain neuronal cell bodies but permit axons and dendrites to cross through (Fig. 1) (38). Adjusting the lengths of microchannels made it possible to allow axons and dendrites from the right (or "postsynaptic") chamber, but only axons from the left (or "presynaptic") chamber to reach the central (or "synaptic") chamber (Fig. 1C) (30). As a novel design feature, one end of the synaptic chamber bifurcates, where one branch terminates with an access well and the other one connects to a fourth (co-culture) chamber *via* a dense series of short microchannels. In addition, we employed narrowing microchannels that promote unidirectional neurite crossing (53). When rat postnatal hippocampal neurons were cultured in one chamber only (Fig. S2), 2.9× more axons crossed the long microchannels in the forward direction (from the wide end towards the narrow end) than the reverse direction. This figure decreased to 1.9× in the case of short microchannels.

At 14 days *in vitro* (DIV14), no dendrites emanating from neurons cultured in the presynaptic chamber were observed in the synaptic chamber. Axons from these neurons, however, invaded the entire synaptic chamber. 11.0%±4.0% of these axons crossed the short microchannels in the reverse direction and reached the postsynaptic chamber, as measured by the ratio of the β3-tubulin fluorescence between the emitting and receiving chambers. On the other hand, axons and dendrites from neurons cultured in the postsynaptic chamber fully invaded the synaptic chamber by DIV14. None of these dendrites and only 5.9%±1.6% of these axons crossed the long microchannels in the reverse direction and reached the presynaptic chamber. Synapse formation in the synapse chamber was confirmed by immunostaining against Synaptophysin (Syp) 1 and Homer 1, pre- and postsynaptic markers, respectively (Fig. 1E). In summary, the synaptic chamber receives axons from both pre- and postsynaptic chambers, receives dendrites only from the postsynaptic chamber, and contains 83.2%±6.1% of all synaptic connections formed between pre- and postsynaptic chambers.

### Effect of synthetic $A\beta_{42}$ oligomers on synapse connectivity

We oligomerized synthetic $A\beta_{1\text{-}42}$ and $A\beta_{42\text{-}1}$ (inverted control peptide) and assessed the presence of oligomeric species *via* Coomassie blue staining. We confirmed the presence of low-MW oligomers in the $A\beta_{1\text{-}42}$ sample (Fig. 2A). We exposed mature synapses (DIV14) to synthetic Aβ peptides by adding the oligomer solution to the synapse chamber to reach an initial concentration of 100 nM. We kept the media levels in the synaptic reservoirs lower than those in the pre- and postsynaptic reservoirs. The hydrostatic pressure difference induced a flow through the microchannels countering the molecular diffusion, which localized the treatment initially to the synaptic chamber. However, as the pressure-driven flow ceased, the media levels equilibrated and Aβ peptides diffused throughout the device. Since the short microchannels offer little fluidic resistance compared to the long microchannels, it would be safe to assume that the media levels equilibrated first between the synaptic and postsynaptic chambers and then between the synaptic and presynaptic chambers.

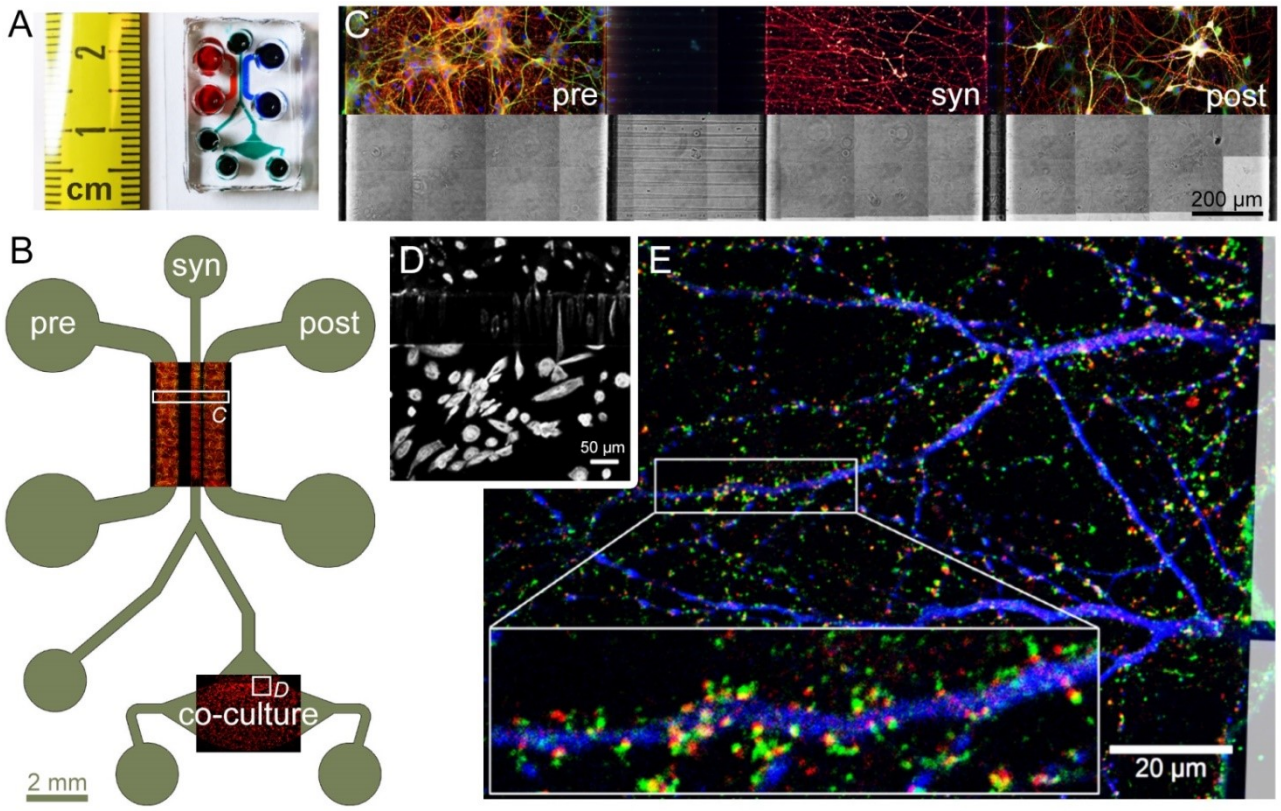


**Figure 1.** Design and operating principle of the microfluidic co-culture device. **A.** Photograph of the microfluidic device bonded to a coverslip. **B.** The layout of the device showing the presynaptic (pre), synaptic (syn), and postsynaptic (post) chambers, as well as the co-culture chamber housing the CHO cells. Overlays show immunofluorescence images of primary neurons and CHO cells in their respective chambers, stained for α-tubulin (red) and MAP2 (green). **C.** Subcellular compartmentalization of neurons was shown by immunostaining against β3-tubulin (red) and MAP2 (green), axonal and somatodendritic markers, respectively. Cell bodies were stained with Hoechst (blue). Microchannel structure is evident in the brightfield image of the same area. **D.** 15× magnification of the square marked in (B), showing CHO cells cultured in the co-culture chamber. CHO cells pass through the microchannels, but do not migrate up the synaptic channel. **E.** Synapse formation in the synaptic chamber was evidenced by the localization of Synaptopysin 1 (green) and Homer 1 (red) puncta, pre- and postsynaptic markers, respectively, around MAP2-positive dendrites (blue). Boxed area is 3× magnified.

At the end of the 16 h treatment period, the neurons were fixed and immunostained against pre- and postsynaptic markers. To quantitatively analyze synaptic connectivity, we developed an image analysis workflow based on scanning confocal microscopy, software-assisted identification of pre- and postsynaptic puncta, and proximity-based assignment of postsynaptic puncta to presynaptic puncta (Fig. S1). Briefly, each Homer spot was assigned to the nearest Syp spot within a cut-off distance, which was pre-determined using a training set (Fig. S1G). The fraction of Syp puncta with at least one Homer assignments and the average number of Homer assignments per Syp were determined to be the most robust read-outs of synapse connectivity. Exposing synapses to synthetic $A\beta_{1\text{-}42}$ oligomers decreased the fraction of assigned Syp without affecting the average number of assignments (Fig. 2B). However, the effect size was small (15.6%) and the variation within and among experiments was high.

### Co-culture with CHO cells expressing human APP with London mutation (V717I) induces synaptotoxicity

We cultured Chinese hamster ovary (CHO) cell lines stably overexpressing human APP, either wild-type ($CHO\text{-}APP^{WT}$) or with V717I (London) mutation ($CHO\text{-}APP^{LDN}$). It has been shown that $CHO\text{-}APP^{WT}$ and $CHO\text{-}APP^{LDN}$ continuously secrete physiologically-relevant forms of Aβ molecules and $CHO\text{-}APP^{LDN}$ provides toxic Aβ species (43). Immunoblot analysis of media collected from CHO cell cultures confirmed

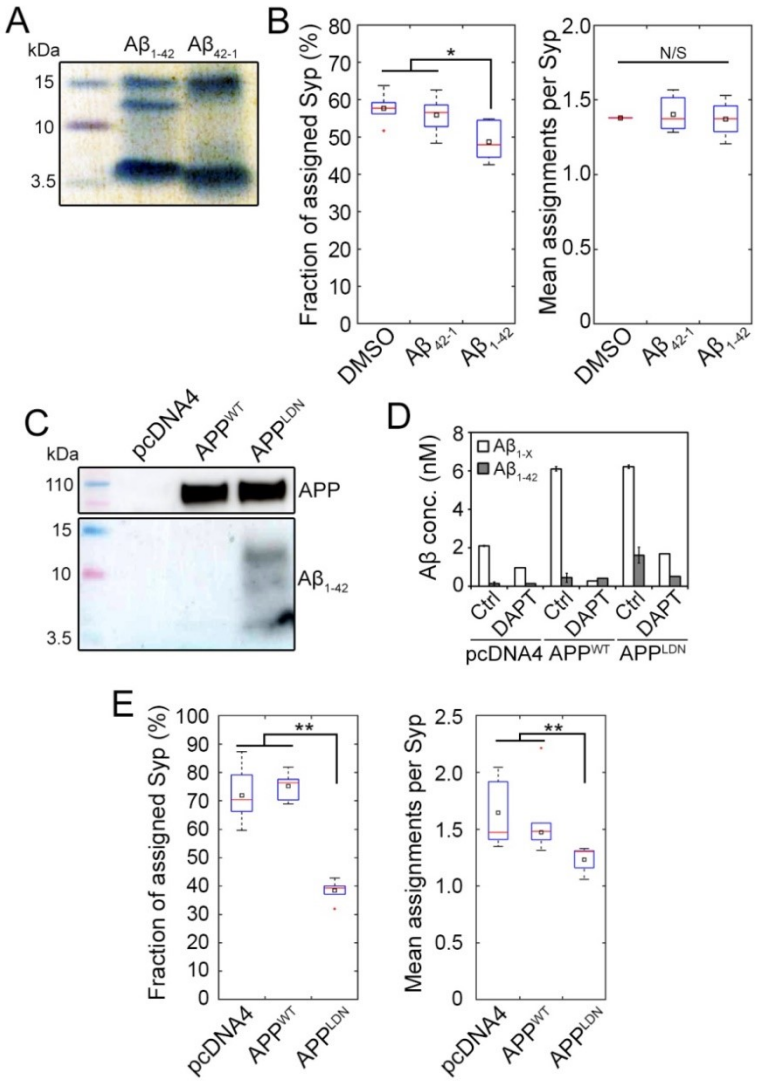


**Figure 2.** Synthetic and cell-secreted $A\beta_{1-42}$ induce different levels of synaptic toxicity. **A.** Coomassie blue stain of in-house oligomerized synthetic $A\beta_{1-42}$ and $A\beta_{42-1}$ (inverted control) peptides show the presence of low molecular weight oligomers. **B.** Synaptic read-outs 16 h after the introduction of synthetic oligomer solution into the synaptic chamber at DIV14 (final concentration = 100 nM). Fraction of Syp puncta assigned by Homer puncta and the mean number of Homer puncta assigned per Syp, according to distance-based analysis workflow (see Fig. S1 for details). **C.** Immunoblots of CHO cell media two days after stimulation. **D.** Alpha-LISA measurement of $A\beta_{1-X}$ and $A\beta_{1-42}$ in media collected from the top well of the synaptic chamber at DIV14. γ-secretase inhibitor DAPT was applied at 18 μg/mL for 5 d. **E.** Synaptic read-outs following co-culture with CHO cells (at DIV 14). In box plots, red bars, black squares, and red plus signs indicate sample median and mean, and outliers, respectively. In panel *B*, N = 5-6 devices from at least 3 independent cultures. In panel *E*, N = 6-7 co-culture devices from 3 independent cultures. Analysis based on 416.3 ± 69.2 Syn puncta per image. Kruskal-Wallis ANOVA, followed by Wilcoxon rank-sum test. * $p < 0.05$; ** $p < 0.005$; N/S: not significant.

that only the peptides secreted by CHO-$APP^{LDN}$ formed low-MW oligomers (Fig. 2C). In contrast, CHO-pcDNA4 cells, which do not overexpress APP, did not produce any Aβ. We conducted off-chip ELISA measurements to determine the relative levels of Aβ species in CHO cell media (Fig. S3). As expected, treatment with the γ-secretase inhibitor DAPT completely blocked the secretion of Aβ peptides by both CHO-$APP^{WT}$ and CHO-$APP^{LDN}$ cells. Moreover, $A\beta_{1-42}$ (but not $A\beta_{1-40}$) levels in CHO-$APP^{LDN}$ media was higher than in CHO-$APP^{WT}$ media, further supporting the immunoblot results.

To determine the effect of CHO cell-secreted Aβ forms on synapses, we plated *ca*. 10,000 CHO cells in the co-culture chamber 4-6 days prior to the primary neuron culture. This timing was necessary to overcome the problems invoked by the differences of growth media composition between CHO cells and primary

neurons. CHO cells proliferated in their growth medium and fully occupied the co-culture chamber. CHO cells were able to cross the short microchannels separating the co-culture chamber from the synaptic chamber (Fig. 1D), but they did not migrate up the synaptic chamber. When the growth medium was replaced with the stimulation medium, the cells stopped proliferating, but continued to secrete Aβ peptides. To confirm that CHO cell-secreted Aβ forms diffused into the synaptic chamber, we collected media from different media reservoirs and quantified their $A\beta_{1\text{-}X}$ and $A\beta_{1\text{-}42}$ peptide content using corresponding Alpha-LISA kits. Note that media collected from the wells of the microfluidic device did not contain sufficient material for immunoblotting. Measurements taken at DIV14 revealed that the ratio of $A\beta_{1\text{-}42}$ to other Aβ forms in the synaptic chamber was 4.4-fold higher in CHO-$APP^{LDN}$ co-cultures than in CHO- $APP^{WT}$ co-cultures (Fig. 2D), as expected for the overexpression of mutated APP (43). Aβ forms in the media decreased to undetectable levels when CHO cells were treated with γ-secretase inhibitor DAPT for 5 d prior to media collection, further confirming that the majority of the measured Aβ in the synaptic chamber was secreted by the CHO cells. Presence of $A\beta_{1\text{-}X}$ in media collected from the synaptic chamber, but not in the co-culture chamber of the CHO-pcDNA4 co-cultures is indicative of neuronal APP processing, since CHO-pcDNA4 cells do not express APP and therefore do not secrete Aβ peptides (Fig. S4).

We conducted off-chip experiments to assess the availability of cell-secreted Aβ forms following the addition of the conditioned media to primary neuron cultures. Alpha-LISA measurements conducted at different time points (from 6 h to 7 d) suggested that Aβ concentrations in the media decreased logarithmically over time (Fig. S5), suggesting that the peptides degraded or consumed by the cells. In contrast, the concentration of synthetic $A\beta_{1\text{-}42}$ peptide did not exhibit such a decrease over time when added to neurons (Fig. S6). These observations further support the idea that cell-secreted Aβ forms need to be periodically resupplied to the neuron culture medium unless a co-culture model is available. When synapses were exposed to CHO cell-secreted Aβ forms for 14 days in the co-culture device, a strong decrease in synapse connectivity was observed in CHO-$APP^{LDN}$, but not in CHO-$APP^{WT}$ co-cultures (Fig. 2E). In this case, *i.e.*, following chronic exposure, the effect size was large (48.9%) and the variation within and among experiments was low. The average number of Homer puncta assigned per Syp puncta was also significantly lower for CHO-$APP^{LDN}$ co-cultures (22.5% decrease compared to CHO-$APP^{WT}$).

**Aβ antibody 3D6 alters the ratio between different Aβ forms and blocks CHO-$APP^{LDN}$-induced synapse loss**

To further characterize the CHO cell-secreted Aβ forms, we tested two monoclonal Aβ antibodies, human SAR228810 (8810; Sanofi; 3 μg/mL) and the mouse version of Bapineuzumab (3D6; Janssen; 3 μg/mL). Both antibodies were developed for passive immunotherapy and tested in clinical trials. 8810 antibody targets soluble protofibrillar and fibrillar species of Aβ and is inactive against Aβ monomers and small oligomeric aggregates (54). In contrast, the 3D6 antibody targets the N-terminal region of Aβ and expected to capture Aβ molecules in the monomeric conformation (55, 56).

We first conducted off-chip experiments where CHO cells were treated with these antibodies (or with 18 μg/mL DAPT as a negative control) for 5 d. Western blots of the conditioned media showed that DAPT treatment eliminated all Aβ secretion and induced a slight increase in the levels of APP (Fig. 3A). However, WBs of conditioned media following DAPT treatment exhibited a 15 kDa band that overlapped with oligomers of low MW $A\beta_{1\text{-}42}$. Treatment with neither antibody affected the presence of low-MW $A\beta_{1\text{-}42}$ forms. Interestingly, the 3D6 antibody induced a strong increase in monomeric $A\beta_{1\text{-}42}$ levels in both CHO-$APP^{WT}$ and CHO-$APP^{LDN}$ media, in accordance with the idea that 3D6 arrests the peptide in monomeric form and precludes oligomer formation.

We next performed Alpha-LISA measurements from media collected from the co-culture chamber, following the treatment of CHO cells with the aforementioned antibodies for 5 d. However, the 3D6 antibody interfered with the Alpha-LISA measurements and could not be reported (no effect was observed for 8810 antibody). We therefore conducted off-chip ELISA measurements in the media of antibody-treated CHO cells. Treatment with either antibody increased $A\beta_{1\text{-}40}$ in both CHO-$APP^{WT}$ and CHO-$APP^{LDN}$ media.

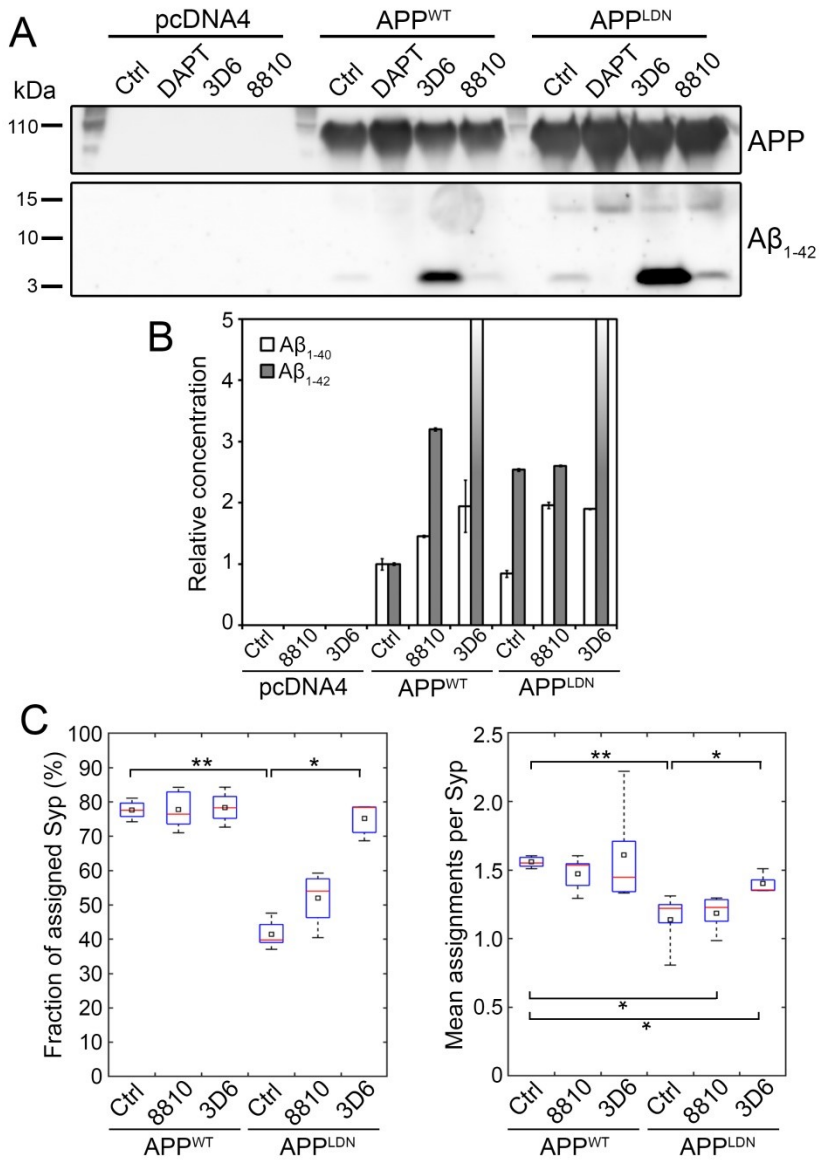


**Figure 3.** Aβ antibody 3D6 modulates Aβ secretion and blocks the synaptotoxicity due to CHO-APP$^{LDN}$ co-culture. **A.** An exemplary immunoblot of CHO cell media collected after 5 day-long treatment with the indicated compounds (DAPT, 18 µg/mL; antibodies, 3 µg/mL) showing APP cleavage products of different molecular weights. **B.** Off-chip ELISA measurements in CHO cell media following antibody treatment. N = 2 independent experiments. Error bars = SEM. **C.** Synaptic read-outs in antibody-treated co-cultures at DIV 14. In box plots, red bars, black squares, and red plus signs indicate sample median and mean, and outliers, respectively. N = 3-5 microfluidic devices from at least 3 independent cultures. Analysis based on 459.5 ± 72.3 Syn puncta per image. Kruskal-Wallis ANOVA, followed by Wilcoxon rank-sum test. * $p < 0.05$; ** $p < 0.01$.

Treatment with 8810 antibody did not affect $A\beta_{1-42}$ concentration in CHO-APP$^{LDN}$ medium, but increased it in CHO-APP$^{WT}$ to the CHO-APP$^{LDN}$ level. In both CHO-APP$^{WT}$ and CHO-APP$^{LDN}$ media, 3D6 antibody treatment caused a decent increase in $A\beta_{1-40}$, but a very large increase in $A\beta_{1-42}$, consistent with the WB data (Fig. 3B). In summary, the 3D6 antibody appears to arrest $A\beta_{1-42}$ peptides in monomeric form, thus leading the accumulation of the signal.

Finally, we analyzed synaptic connectivity in co-cultures treated with 8810 and 3D6 antibodies for 5 d prior to fixation (Fig. 3C). Similar to Fig. 2E, untreated CHO-APP$^{LDN}$ co-cultures exhibited a strong (46.6%) decrease in the fraction of Syp puncta assigned by Homer puncta and a significant decrease (26.9%) in the number of Homer assignments per Syp. Treatment with 8810 antibody did not induce a significant difference relative to untreated controls in both cell types. However, treatment with 3D6 antibody completely blocked the effect of CHO-APP$^{LDN}$ on the fraction of Syp assigned and partially blocked the effect of CHO-APP$^{LDN}$

on the number of assignment per Syp. In summary, treatment with an antibody that prevents Aβ monomers from forming oligomers interfered with CHO-APP$^{LDN}$-secreted Aβ species and protected synapses from toxicity likely induced by low-MW oligomers. These findings highlight the potential use of our disease-on-a-chip model and synaptic connectivity analysis for assessing the synapto-protective effects of therapeutic compounds for AD, such as Aβ-targeting antibodies.

**Pyk2 overexpression in "postsynaptic" neurons blocks CHO-APP$^{LDN}$-induced decrease in synapse connectivity**

We next assessed the relevance of our microfluidic tool to establish whether genetic risk factors of AD may be involved in Aβ-dependent synaptotoxicity. Several lines of evidence indicate that genetically driven synaptic failure may occur in AD (25) and among the different genetic risk factors susceptible to be studied in our model we focused on *PTK2B* which has been already described to be involved in synaptic functions (20).

We evaluated potential changes in the expression of *PTK2B* in the brains of AD patients compared to healthy individuals by taking advantage of three publicly available RNAseq datasets: Mayo Clinic data that probed the temporal cortex (47); ROSMAP data that probed the dorsolateral prefrontal cortex (46); and the MSBB data that probed four different brain areas: BA 10, BA 22, BA 36, and BA 44 (45). This allowed us to investigate potential gene expression changes in brain regions that are affected at different pathological stages of AD (57). We observed a decrease in *PTK2B* expression in AD cases compared to healthy controls in all brain regions analyzed (Table S2); however, after multiple testing correction this decrease was significant only in the BA 22 (16.69% decrease; $p_{adj} = 1.99\times10^{-02}$), BA 36 (28.89% decrease; $p_{adj} = 8.49\times10^{-05}$), and BA 44 (15.18% decrease; $p_{adj} = 3.87\times10^{-02}$) regions of the MSBB dataset, as well as in the ROSMAP dataset (28.89% decrease; $p_{adj} = 4.57\times10^{-03}$). Consistent with these results, we observed a decreasing trend in Pyk2 total protein levels and an increasing trend in the p-Pyk2 protein levels in the brains of AD patients compared to healthy controls (Fig. S7). These changes resulted in an increase in the relative phosphorylation of Pyk2 in the hippocampus (4.1-fold increase in the p-Pyk2:Pyk2 ratio; p = 0.0274; Wilcoxon rank sum test; 17 cases vs. 6 controls) and in the cortex (3.6-fold increase in the p-Pyk2:Pyk2 ratio; p = 0.0274; Wilcoxon rank sum test; 17 cases vs. 7 controls), suggesting a compensatory mechanism.

We then evaluated the levels of Pyk2 and phospho-Pyk2 in primary neurons as a function of Aβ exposure. We conducted off-chip synaptosome extraction using primary cortical neurons treated with CHO cell media (Fig. 4B). We observed total Pyk2 and p-Pyk2 in both non-PSD and PSD fractions. Syp and PSD95 signals were not different between neurons treated with CHO-APP$^{WT}$ medium and neurons treated with CHO-APP$^{LDN}$ medium (Fig. S9); however, CHO-APP$^{LDN}$ medium caused significant decreases in the relative amounts of total Pyk2 and p-Pyk2 in the postsynaptic fraction (Fig. 4B).When p-Pyk2 (Tyr402) was immunostained alongside synaptic markers, we observed that signals localized to both pre- and postsynaptic puncta, with an increased tendency towards the latter (Fig. 4A). We extended our distance-based synaptic connectivity analysis to quantitatively analyze the distribution of p-Pyk2 signals relative to identified synapses, *i.e.*, Syp–Homer pairs. Our data showed that 1.5-fold more p-Pyk2 puncta were localized near postsynaptic puncta than near presynaptic puncta regardless of co-culture with CHO-APP$^{WT}$ or CHO-APP$^{LDN}$ cells (Fig. S8).

Since we observed (i) a decrease in *PTK2B* expression and a decreasing trend in Pyk2 protein levels in AD brains, (ii) a decrease in Pyk2 levels in the PSD fraction of cortical neurons upon treatment with CHO-APP$^{LDN}$ media, and (iii) a decrease in synaptic connectivity in hippocampal neurons upon co-culture with CHO-APP$^{LDN}$ cells, we hypothesized that Pyk2 was protective and its overexpression could rescue the detrimental effect of CHO-APP$^{LDN}$ co-culture on synapses. Since the active form of Pyk2 was strongly associated with postsynapses and CHO-APP$^{LDN}$ medium affected Pyk2 levels specifically in the PSD fraction, we decided to take advantage of microfluidic compartmentalization and modulate Pyk2 expression in postsynaptic neurons. To this end, we first verified the overexpression of Pyk2 off-chip *via* lentiviral transduction of the relevant shRNA or cDNA, respectively (Fig. S10). Next, by using lentiviruses expressing

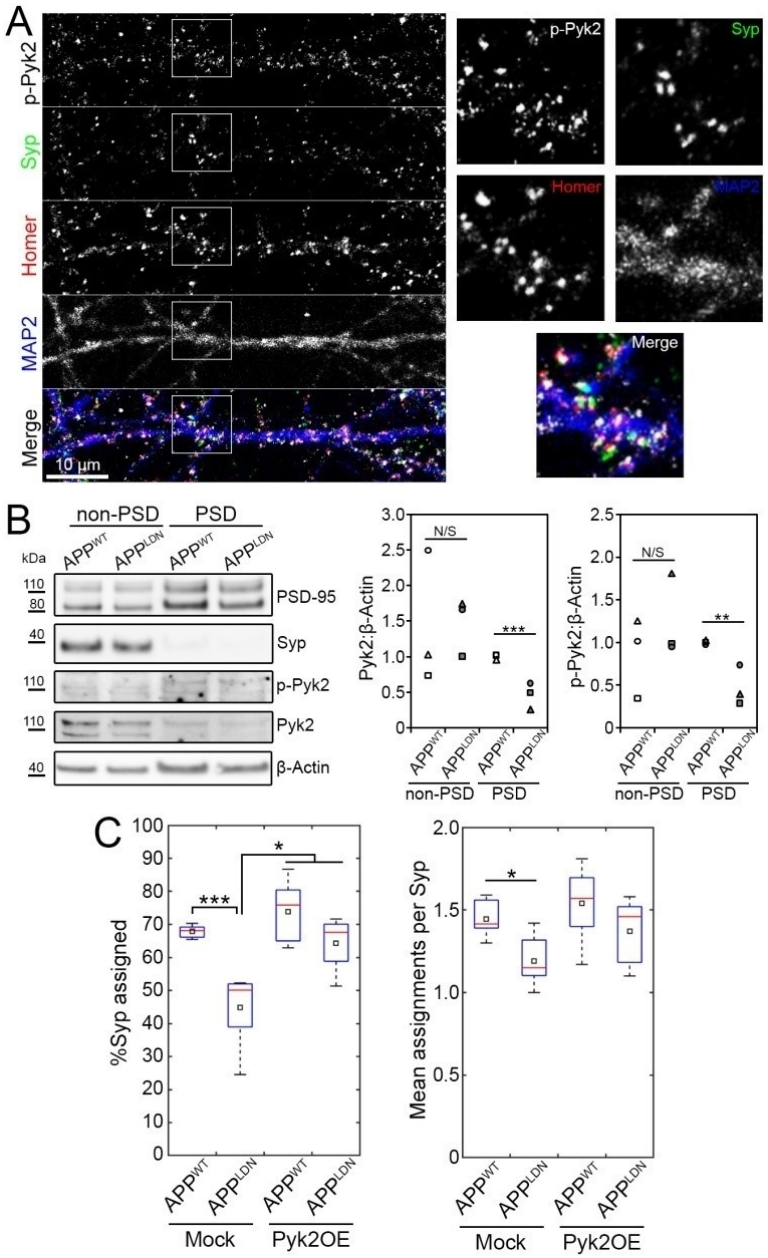


**Figure 4.** Pyk2 overexpression in postsynaptic neurons blocks the synaptotoxicity due to CHO-APP$^{LDN}$ co-culture. **A.** An exemplary immunofluorescence image of the synaptic chamber at DIV14 showing phospho-Pyk2 Tyr402 (p-Pyk2), Synaptophysin 1 (Syp) Homer 1, and MAP2. Boxed areas are 2.4× magnified. **B.** Exemplary immunoblots and quantification of the postsynaptic (PSD) fraction following synaptosome extraction at DIV14 following 16 h-long treatment with the indicated CHO cell medium. N = 3 independent experiments. Student's *t*-test **C.** Synaptic read-outs following Pyk2 overexpression in postsynaptic neurons from DIV7 to DIV14. In box plots, red bars and black squares indicate sample median and mean, respectively. N = 5-7 devices from 3 independent experiments. Kruskal-Wallis ANOVA, followed by Wilcoxon rank-sum test. Error bars = SEM. * $p < 0.05$; ** $p < 0.01$; *** $p < 0.005$; N/S: not significant.

fluorescent proteins, we confirmed that the transduction was restricted to the target chamber (selectively to pre- or postsynaptic chambers; Fig. S11). Over-expression of Pyk2 in the postsynaptic chamber blocked the detrimental effect of CHO-APP$^{LDN}$ co-culture on synaptic connectivity, as evidenced by 12.9% decrease in the fraction of Syp puncta assigned by Homer puncta (as compared to 33.9% decrease when overexpressing the control vector; Fig. 4C). As expected, synaptic connectivity in CHO-APP$^{WT}$ co-cultures was not affected by Pyk2 overexpression (8.7% increase in the fraction of Syp assigned by Homer), confirming that the synaptoprotective effect of postsynaptic Pyk2 overexpression was specific to Aβ toxicity due to CHO-APP$^{LDN}$ co-culture.

## Discussion

The use of microfluidic culture devices for isolating synapses from neuronal cell bodies has been previously demonstrated (30, 31). Our co-culture device combines two design concepts: First, by employing different microchannel lengths, it guarantees that dendrites from one but not the other neuron chamber can arrive to the synapse chamber. Second, it minimizes the penetration of axons from the synapse chamber to the neuron chambers. Our co-culture device facilitated the passage of axons in the intended direction: 2.9× and 1.9× more axons crossed the microchannels in the intended direction relative to the reverse direction, respectively for long and short microchannels. These ratios are indicative of a limited effect of the narrowing channel design on hippocampal neurons and are consistent with earlier reports (53). Our co-culture device also facilitated the concentration of synapses in the synapse chamber: More than 83% of all synapses formed between neurons cultured in the pre- and postsynaptic chambers were found in the synapse chamber. It therefore provides a simple yet robust method to treat and analyze synapses independent of the cell bodies. It is important to note that while all dendrites in the synapse chamber arrive from the postsynaptic chamber, the opposite statement is not true, *i.e.*, not all axons in the synapse chamber arrive from the presynaptic chamber. Thus, overexpressing Pyk2 in the postsynaptic chamber guarantees that, for all synapses analyzed, Pyk2 is overexpressed in the postsynaptic neuron (if we assume 100% transduction efficiency); however, it cannot be known whether or not Pyk2 is also overexpressed in the presynaptic neuron.

Several parameters can be considered when inducing Aβ-dependent synaptotoxicity: (i) use of synthetic versus organic oligomers; (ii) acute versus chronic treatment. Our microfludic co-culture model combines organic oligomers at physiological concentrations with chronic treatments and consistently induces Aβ-dependent synaptotoxicity. This is in agreement with a recent report that synthetic oligomers do not assume the same molecular structure as organic oligomers,(26) suggesting potential differences in their biological effects. Interestingly, as opposed to synthetic Aβ oligomers, organic Aβ appears to be degraded in our primary neuronal cultures, further highlighting the difference in bioavailability between the two. This observation also indicates that the co-culture model is better adapted for synaptotoxicity studies since it maintains physiological concentrations thanks to the constant release of Aβ peptides from CHO cells. This allows for the analysis of synapse connectivity in response to chronic exposure of synapses to organic Aβ oligomers, as opposed to acute exposure to conditioned media, for instance.

It is important to note that the Aβ peptides secreted by the CHO-APP$^{LDN}$ cells do diffuse into the various chambers of the microfluidic device, considering the long duration of co-culture experiments. Thus, the synaptic toxicity observed may not be due to a local effect on synapses, but originate from Aβ's toxic effect on neuronal cell bodies. If true, this is more likely due to toxicity on neurons in the postsynaptic neurons, as the fluidic barrier between the synaptic and postsynaptic chambers is much weaker than that between the synaptic and presynaptic chambers. Regardless of this possibility, our results do not allow us to propose a specific mechanism for the observed Aβ-induced synaptotoxicity.

The role of Pyk2 in synapses appears to be complex, considering the seemingly opposite results of recent studies: Pyk2 has been shown to be required for long-term potentiation (LTP) (28). However, others have shown that Pyk2 is not required for LTP, but for long-term depression (23, 58), and Pyk2 overexpression inhibits LTP (58). The role of Pyk2 in Aβ toxicity has also been debated, where it has been shown to be deleterious (23) or protective (29) in mouse models. Our findings are in agreement with the notion that Pyk2 localizes to the postsynaptic compartment (20). At the AD pathophysiological level, several of our observations fit well with the results of a recent *in vivo* study using AD-like mouse models: (i) decreased Pyk2 activity has been reported in 5XFAD mice (29), although Pyk2 has also been shown to be activated in acute Aβ oligomer treatment on brain slices (59, 60); (ii) rescue of Pyk2 expression improved the behavioral and synaptic molecular phenotypes of the double transgenic 5XFAD×Pyk$^{-/-}$ mouse model (29). Interestingly, this rescue seems to have no impact on Aβ loads, suggesting that Pyk2 overexpression impacts pathophysiological processes downstream of Aβ production and amyloid deposition. This observation is in agreement with our results suggesting that Pyk2 overexpression may restrict Aβ-induced synaptotoxicity.

Nevertheless, it is important to mention that the sparse literature on Pyk2's role in synapses is highly dependent on the model and calls for further *in vitro* and *in vivo* work.

## Conclusions

In conclusion, our microfluidic co-culture device provides an *in vitro* model of Aβ synaptotoxicity based on exposing synapses of primary hippocampal neurons to cell-secreted $A\beta_{1-42}$ peptides. This disease-on-a-chip model is highly relevant to AD in several aspects: (i) long-term, low-dose exposure to organic Aβ forms is preferable over acute treatments with synthetic oligomers at high concentrations; (ii) isolating synapses in a separate microfluidic chamber facilitates the analysis of synaptic connectivity *via* immunostaining pre- and postsynaptic markers without the interference of cell bodies; (iii) providing exclusive access to pre- and postsynaptic neurons to selectively under- or overexpress AD genetic risk factors therein helps dissect their potential roles in pre- and postsynaptic compartments. Deciphering the mechanisms by which the genetic risk factors contribute to AD pathology will help develop targeted therapies based on genetic information.

## Acknowledgements

This work was partly supported by the French RENATECH network (P-16-01891). This study was funded by INSERM, Institut Pasteur de Lille, the EU Joint Programme – Neurodegenerative Diseases Research (JPND; 3DMiniBrain), Agence Nationale de la Recherche (ANR-19-CE16-0020), and Fondation Vaincre Alzheimer (FR-17006p). This work was also funded by the Lille Métropole Communauté Urbaine and the French government's LABEX DISTALZ program (Development of innovative strategies for a transdisciplinary approach to Alzheimer's disease). D. M.-C. was supported by a PhD scholarship from Coordenação de Aperfeiçoamento de Pessoal de Nível Superior (CAPES). This work was also co-funded by the European Union under the European Regional Development Fund (ERDF) and by the Hauts de France Regional Council (contract no. 18006176), the Métropole Européenne de Lille (contract no. 2016_ESR_05), and the French State (contract no. 2018-3-CTRL_IPL_Phase2). The aforementioned funding bodies did not play any roles in the design of the study and collection, analysis, and interpretation of data and in writing the manuscript.

The authors thank the BICeL platform of the Institut Biologie de Lille. The authors thank Laurent Pradier and Philippe Bertrand at Sanofi for fruitful discussions. The authors thank Karine Blary at the IEMN Lille for the microfabrication work. The authors thank the vectorology platform Transbiomed for lentivirus production. The authors thank Charles Duyckaerts and the "NeuroCEB" Brain Bank (GIE Neuro-CEB BB-0033-00011) for providing the brain tissue samples.

The results published here are in whole or in part based on data obtained from the AMP-AD Knowledge Portal (https://adknowledgeportal.synapse.org/).

These data were generated from postmortem brain tissue collected through the Mount Sinai VA Medical Center Brain Bank and were provided by Dr. Eric Schadt from Mount Sinai School of Medicine.

Study data were also provided by the following sources: The Mayo Clinic Alzheimers Disease Genetic Studies, led by Dr. Nilufer Taner and Dr. Steven G. Younkin, Mayo Clinic, Jacksonville, FL using samples from the Mayo Clinic Study of Aging, the Mayo Clinic Alzheimers Disease Research Center, and the Mayo Clinic Brain Bank. Data collection was supported through funding by NIA grants P50 AG016574, R01 AG032990, U01 AG046139, R01 AG018023, U01 AG006576, U01 AG006786, R01 AG025711, R01 AG017216, R01 AG003949, NINDS grant R01 NS080820, CurePSP Foundation, and support from Mayo Foundation. Study data includes samples collected through the Sun Health Research Institute Brain and Body Donation Program of Sun City, Arizona. The Brain and Body Donation Program is supported by the National Institute of Neurological Disorders and Stroke (U24 NS072026 National Brain and Tissue Resource for Parkinsons Disease and Related Disorders), the National Institute on Aging (P30 AG19610 Arizona Alzheimers Disease Core Center), the Arizona Department of Health Services (contract 211002, Arizona

Alzheimers Research Center), the Arizona Biomedical Research Commission (contracts 4001, 0011, 05-901 and 1001 to the Arizona Parkinson's Disease Consortium) and the Michael J. Fox Foundation for Parkinsons Research.

Study data were also provided by the Rush Alzheimer's Disease Center, Rush University Medical Center, Chicago. Data collection was supported through funding by NIA grants P30AG10161 (ROS), R01AG15819 (ROSMAP; genomics and RNAseq), R01AG17917 (MAP), R01AG30146, R01AG36042 (5hC methylation, ATACseq), RC2AG036547 (H3K9Ac), R01AG36836 (RNAseq), R01AG48015 (monocyte RNAseq) RF1AG57473 (single nucleus RNAseq), U01AG32984 (genomic and whole exome sequencing), U01AG46152 (ROSMAP AMP-AD, targeted proteomics), U01AG46161(TMT proteomics), U01AG61356 (whole genome sequencing, targeted proteomics, ROSMAP AMP-AD), the Illinois Department of Public Health (ROSMAP), and the Translational Genomics Research Institute (genomic). Additional phenotypic data can be requested at www.radc.rush.edu.

## References

1. Nisbet RM, Polanco JC, Ittner LM, Gotz J. Tau aggregation and its interplay with amyloid-beta. Acta Neuropathol. 2015;129:207-20.
2. De Strooper B. Proteases and proteolysis in Alzheimer disease: a multifactorial view on the disease process. Physiol Rev. 2010;90:465-94.
3. Hardy J, Selkoe DJ. The amyloid hypothesis of Alzheimer's disease: progress and problems on the road to therapeutics. Science. 2002;297:353-6.
4. Stine WB, Jr., Dahlgren KN, Krafft GA, LaDu MJ. In vitro characterization of conditions for amyloid-beta peptide oligomerization and fibrillogenesis. J Biol Chem. 2003;278:11612-22.
5. Dahlgren KN, Manelli AM, Stine WB, Jr., Baker LK, Krafft GA, LaDu MJ. Oligomeric and fibrillar species of amyloid-beta peptides differentially affect neuronal viability. J Biol Chem. 2002;277:32046-53.
6. Resende R, Ferreiro E, Pereira C, Resende de Oliveira C. Neurotoxic effect of oligomeric and fibrillar species of amyloid-beta peptide 1-42: involvement of endoplasmic reticulum calcium release in oligomer-induced cell death. Neuroscience. 2008;155:725-37.
7. Deshpande A, Mina E, Glabe C, Busciglio J. Different conformations of amyloid beta induce neurotoxicity by distinct mechanisms in human cortical neurons. J Neurosci. 2006;26:6011-8.
8. Ferreira IL, Bajouco LM, Mota SI, Auberson YP, Oliveira CR, Rego AC. Amyloid beta peptide 1-42 disturbs intracellular calcium homeostasis through activation of GluN2B-containing N-methyl-d-aspartate receptors in cortical cultures. Cell Calcium. 2012;51:95-106.
9. Spires-Jones TL, Hyman BT. The intersection of amyloid beta and tau at synapses in Alzheimer's disease. Neuron. 2014;82:756-71.
10. Benilova I, Karran E, De Strooper B. The toxic Abeta oligomer and Alzheimer's disease: an emperor in need of clothes. Nat Neurosci. 2012;15:349-57.
11. Brody AH, Strittmatter SM. Synaptotoxic Signaling by Amyloid Beta Oligomers in Alzheimer's Disease Through Prion Protein and mGluR5. Adv Pharmacol. 2018;82:293-323.
12. Lansbury PT, Jr. Evolution of amyloid: what normal protein folding may tell us about fibrillogenesis and disease. Proc Natl Acad Sci U S A. 1999;96:3342-4.
13. Scheff SW, Price DA, Schmitt FA, DeKosky ST, Mufson EJ. Synaptic alterations in CA1 in mild Alzheimer disease and mild cognitive impairment. Neurology. 2007;68:1501-8.
14. Sepulveda FJ, Parodi J, Peoples RW, Opazo C, Aguayo LG. Synaptotoxicity of Alzheimer beta amyloid can be explained by its membrane perforating property. PLoS One. 2010;5:e11820.
15. Hong S, Beja-Glasser VF, Nfonoyim BM, Frouin A, Li S, Ramakrishnan S, et al. Complement and microglia mediate early synapse loss in Alzheimer mouse models. Science. 2016;352:712-6.
16. Um JW, Nygaard HB, Heiss JK, Kostylev MA, Stagi M, Vortmeyer A, et al. Alzheimer amyloid-beta oligomer bound to postsynaptic prion protein activates Fyn to impair neurons. Nat Neurosci. 2012;15:1227-35.

17. Wang Q, Walsh DM, Rowan MJ, Selkoe DJ, Anwyl R. Block of long-term potentiation by naturally secreted and synthetic amyloid beta-peptide in hippocampal slices is mediated via activation of the kinases c-Jun N-terminal kinase, cyclin-dependent kinase 5, and p38 mitogen-activated protein kinase as well as metabotropic glutamate receptor type 5. J Neurosci. 2004;24:3370-8.

18. Kunkle BW, Grenier-Boley B, Sims R, Bis JC, Damotte V, Naj AC, et al. Genetic meta-analysis of diagnosed Alzheimer's disease identifies new risk loci and implicates Abeta, tau, immunity and lipid processing. Nat Genet. 2019;51:414-30.

19. Lambert JC, Ibrahim-Verbaas CA, Harold D, Naj AC, Sims R, Bellenguez C, et al. Meta-analysis of 74,046 individuals identifies 11 new susceptibility loci for Alzheimer's disease. Nat Genet. 2013;45:1452-8.

20. Giralt A, Brito V, Chevy Q, Simonnet C, Otsu Y, Cifuentes-Diaz C, et al. Pyk2 modulates hippocampal excitatory synapses and contributes to cognitive deficits in a Huntington's disease model. Nat Commun. 2017;8:15592.

21. Ojelade SA, Lee TV, Giagtzoglou N, Yu L, Ugur B, Li Y, et al. cindr, the Drosophila Homolog of the CD2AP Alzheimer's Disease Risk Gene, Is Required for Synaptic Transmission and Proteostasis. Cell Rep. 2019;28:1799-813.e5.

22. Schurmann B, Bermingham DP, Kopeikina KJ, Myczek K, Yoon S, Horan KE, et al. A novel role for the late-onset Alzheimer's disease (LOAD)-associated protein Bin1 in regulating postsynaptic trafficking and glutamatergic signaling. Mol Psychiatry. 2019.

23. Salazar SV, Cox TO, Lee S, Brody AH, Chyung AS, Haas LT, et al. Alzheimer's Disease Risk Factor Pyk2 Mediates Amyloid-beta-Induced Synaptic Dysfunction and Loss. J Neurosci. 2019;39:758-72.

24. Eysert F, Coulon A, Boscher E, Vreulx AC, Flaig A, Mendes T, et al. Alzheimer’s genetic risk factor FERMT2 (Kindlin-2) controls axonal growth and synaptic plasticity in an APP-dependent manner. bioRxiv. 2019:767194.

25. Dourlen P, Kilinc D, Malmanche N, Chapuis J, Lambert JC. The new genetic landscape of Alzheimer's disease: from amyloid cascade to genetically driven synaptic failure hypothesis? Acta Neuropathol. 2019;138:221-36.

26. Kollmer M, Close W, Funk L, Rasmussen J, Bsoul A, Schierhorn A, et al. Cryo-EM structure and polymorphism of Abeta amyloid fibrils purified from Alzheimer's brain tissue. Nat Commun. 2019;10:4760.

27. Bartos JA, Ulrich JD, Li H, Beazely MA, Chen Y, Macdonald JF, et al. Postsynaptic clustering and activation of Pyk2 by PSD-95. J Neurosci. 2010;30:449-63.

28. Huang Y, Lu W, Ali DW, Pelkey KA, Pitcher GM, Lu YM, et al. CAKbeta/Pyk2 kinase is a signaling link for induction of long-term potentiation in CA1 hippocampus. Neuron. 2001;29:485-96.

29. Giralt A, de Pins B, Cifuentes-Diaz C, Lopez-Molina L, Farah AT, Tible M, et al. PTK2B/Pyk2 overexpression improves a mouse model of Alzheimer's disease. Exp Neurol. 2018;307:62-73.

30. Taylor AM, Dieterich DC, Ito HT, Kim SA, Schuman EM. Microfluidic local perfusion chambers for the visualization and manipulation of synapses. Neuron. 2010;66:57-68.

31. Virlogeux A, Moutaux E, Christaller W, Genoux A, Bruyere J, Fino E, et al. Reconstituting Corticostriatal Network on-a-Chip Reveals the Contribution of the Presynaptic Compartment to Huntington's Disease. Cell Rep. 2018;22:110-22.

32. Chang KH, Vincent F, Shah K. Deregulated Cdk5 triggers aberrant activation of cell cycle kinases and phosphatases inducing neuronal death. J Cell Sci. 2012;125:5124-37.

33. Mairet-Coello G, Courchet J, Pieraut S, Courchet V, Maximov A, Polleux F. The CAMKK2-AMPK kinase pathway mediates the synaptotoxic effects of Abeta oligomers through Tau phosphorylation. Neuron. 2013;78:94-108.

34. Walsh DT, Montero RM, Bresciani LG, Jen AY, Leclercq PD, Saunders D, et al. Amyloid-beta peptide is toxic to neurons in vivo via indirect mechanisms. Neurobiol Dis. 2002;10:20-7.

35. Xiong K, Cai H, Luo XG, Struble RG, Clough RW, Yan XX. Mitochondrial respiratory inhibition and oxidative stress elevate beta-secretase (BACE1) proteins and activity in vivo in the rat retina. Exp Brain Res. 2007;181:435-46.

36. Kelly BL, Ferreira A. Beta-amyloid disrupted synaptic vesicle endocytosis in cultured hippocampal neurons. Neuroscience. 2007;147:60-70.

37. Kuperstein I, Broersen K, Benilova I, Rozenski J, Jonckheere W, Debulpaep M, et al. Neurotoxicity of Alzheimer's disease Abeta peptides is induced by small changes in the Abeta42 to Abeta40 ratio. Embo J. 2010;29:3408-20.

38. Kilinc D, Blasiak A, O'Mahony JJ, Lee GU. Low piconewton towing of CNS axons against diffusing and surface-bound repellents requires the inhibition of motor protein-associated pathways. Sci Rep. 2014;4:7128.

39. Kilinc D, Schwab J, Rampini S, Ikpekha OW, Thampi A, Blasiak A, et al. A microfluidic dual gradient generator for conducting cell-based drug combination assays. Integr Biol (Camb). 2016;8:39-49.

40. Blasiak A, Lee GU, Kilinc D. Neuron subpopulations with different elongation rates and DCC dynamics exhibit distinct responses to isolated netrin-1 treatment. ACS Chem Neurosci. 2015;6:1578-90.

41. Sartori M, Mendes T, Desai S, Lasorsa A, Herledan A, Malmanche N, et al. BIN1 recovers tauopathy-induced long-term memory deficits in mice and interacts with Tau through Thr(348) phosphorylation. Acta Neuropathol. 2019;138:631-52.

42. Chapuis J, Flaig A, Grenier-Boley B, Eysert F, Pottiez V, Deloison G, et al. Genome-wide, high-content siRNA screening identifies the Alzheimer's genetic risk factor FERMT2 as a major modulator of APP metabolism. Acta Neuropathol. 2017;133:955-66.

43. Guillot-Sestier MV, Sunyach C, Ferreira ST, Marzolo MP, Bauer C, Thevenet A, et al. alpha-Secretase-derived fragment of cellular prion, N1, protects against monomeric and oligomeric amyloid beta (Abeta)-associated cell death. J Biol Chem. 2012;287:5021-32.

44. Frandemiche ML, De Seranno S, Rush T, Borel E, Elie A, Arnal I, et al. Activity-dependent tau protein translocation to excitatory synapse is disrupted by exposure to amyloid-beta oligomers. J Neurosci. 2014;34:6084-97.

45. Wang M, Beckmann ND, Roussos P, Wang E, Zhou X, Wang Q, et al. The Mount Sinai cohort of large-scale genomic, transcriptomic and proteomic data in Alzheimer's disease. Sci Data. 2018;5:180185.

46. De Jager PL, Ma Y, McCabe C, Xu J, Vardarajan BN, Felsky D, et al. A multi-omic atlas of the human frontal cortex for aging and Alzheimer's disease research. Sci Data. 2018;5:180142.

47. Allen M, Carrasquillo MM, Funk C, Heavner BD, Zou F, Younkin CS, et al. Human whole genome genotype and transcriptome data for Alzheimer's and other neurodegenerative diseases. Sci Data. 2016;3:160089.

48. Synapse collaborative research platform. https://www.synapse.org/. Accessed 16 March 2020.

49. Bray NL, Pimentel H, Melsted P, Pachter L. Near-optimal probabilistic RNA-seq quantification. Nat Biotechnol. 2016;34:525-7.

50. Love MI, Huber W, Anders S. Moderated estimation of fold change and dispersion for RNA-seq data with DESeq2. Genome Biol. 2014;15:550.

51. Thierry M, Boluda S, Delatour B, Marty S, Seilhean D, Letournel F, et al. Human subiculo-fornico-mamillary system in Alzheimer's disease: Tau seeding by the pillar of the fornix. Acta Neuropathol. 2020;139:443-61.

52. Braak H, Alafuzoff I, Arzberger T, Kretzschmar H, Del Tredici K. Staging of Alzheimer disease-associated neurofibrillary pathology using paraffin sections and immunocytochemistry. Acta Neuropathol. 2006;112:389-404.

53. Peyrin JM, Deleglise B, Saias L, Vignes M, Gougis P, Magnifico S, et al. Axon diodes for the reconstruction of oriented neuronal networks in microfluidic chambers. Lab Chip. 2011;11:3663-73.

54. Santin MD, Vandenberghe ME, Herard AS, Pradier L, Cohen C, Debeir T, et al. In Vivo Detection of Amyloid Plaques by Gadolinium-Stained MRI Can Be Used to Demonstrate the Efficacy of an Anti-amyloid Immunotherapy. Front Aging Neurosci. 2016;8:55.

55. Vandenberghe R, Rinne JO, Boada M, Katayama S, Scheltens P, Vellas B, et al. Bapineuzumab for mild to moderate Alzheimer's disease in two global, randomized, phase 3 trials. Alzheimers Res Ther. 2016;8:18.

56. Miles LA, Crespi GA, Doughty L, Parker MW. Bapineuzumab captures the N-terminus of the Alzheimer's disease amyloid-beta peptide in a helical conformation. Sci Rep. 2013;3:1302.

57. Braak H, Braak E. Demonstration of amyloid deposits and neurofibrillary changes in whole brain sections. Brain Pathol. 1991;1:213-6.

58. Hsin H, Kim MJ, Wang CF, Sheng M. Proline-rich tyrosine kinase 2 regulates hippocampal long-term depression. J Neurosci. 2010;30:11983-93.

59. Haas LT, Salazar SV, Kostylev MA, Um JW, Kaufman AC, Strittmatter SM. Metabotropic glutamate receptor 5 couples cellular prion protein to intracellular signalling in Alzheimer's disease. Brain. 2016;139:526-46.

60. Haas LT, Strittmatter SM. Oligomers of Amyloid beta Prevent Physiological Activation of the Cellular Prion Protein-Metabotropic Glutamate Receptor 5 Complex by Glutamate in Alzheimer Disease. J Biol Chem. 2016;291:17112-21.

**Table S1.** Demographic details of the neuropathological cohort. ND: Not determined.

| *Individual* | *Braak stage* | *Gender* | *Age at death* | *Post-mortem delay (h)* | *Neuropathological diagnosis* |
|---|---|---|---|---|---|
| 1 | 3 | F | 95 | ND | Non-AD |
| 2 | 0 | F | 52 | 29 | Non-AD |
| 3 | 1 | F | 92 | 21 | Non-AD |
| 4 | 2 | M | 82 | 63 | Non-AD |
| 5 | 2 | F | 83 | 21 | Non-AD |
| 6 | 3 | F | 93 | 24 | Non-AD |
| 7 | 0 | M | 69 | 6 | Non-AD |
| 8 | 4 | F | 76 | 28 | Non-AD |
| 9 | 6 | F | 48 | ND | AD |
| 10 | 6 | M | 57 | 19 | AD |
| 11 | 6 | F | 60 | ND | AD |
| 12 | 6 | M | 72 | 44 | AD |
| 13 | 6 | F | 72 | 5 | AD |
| 14 | 6 | F | 78 | 24 | AD |
| 15 | 6 | M | 81 | 17 | AD |
| 16 | 6 | F | 85 | 31 | AD |
| 17 | 6 | F | 100 | 67 | AD |
| 18 | 6 | M | 67 | 30 | AD |
| 19 | 6 | M | 67 | ND | AD |
| 20 | 6 | M | 53 | ND | AD |
| 21 | 6 | F | 56 | 26 | AD |
| 22 | 6 | F | 70 | ND | AD |
| 23 | 6 | M | 76 | 27 | AD |
| 24 | 6 | F | 77 | 48 | AD |
| 25 | 6 | F | 81 | 41 | AD |
| 26 | 6 | F | 85 | 28 | AD |
| 27 | 6 | F | 90 | 24 | AD |

**Table S2.** *PTK2B* gene expression analysis in different publicly-available datasets

| *Dataset* | *Brain region* | *Sample size* | | *Gene expression (ENSG00000120899.17)* | |
|---|---|---|---|---|---|
| | | **AD cases** | **Controls** | **$\log_2$ fold change** | $p_{adj}$ |
| Mayo Clinic | Temporal cortex | 82 | 78 | −0.2036 | 0.1308 |
| Mount Sinai Brain Bank | BA 10 | 105 | 71 | −0.0932 | 0.2802 |
| | BA 22 | 98 | 61 | −0.2635 | 0.0199 |
| | BA 36 | 88 | 64 | −0.4919 | 8.49E-05 |
| | BA 44 | 90 | 63 | −0.2375 | 0.0387 |
| ROSMAP | Dorsolateral prefrontal cortex | 222 | 201 | −0.1577 | 0.0046 |

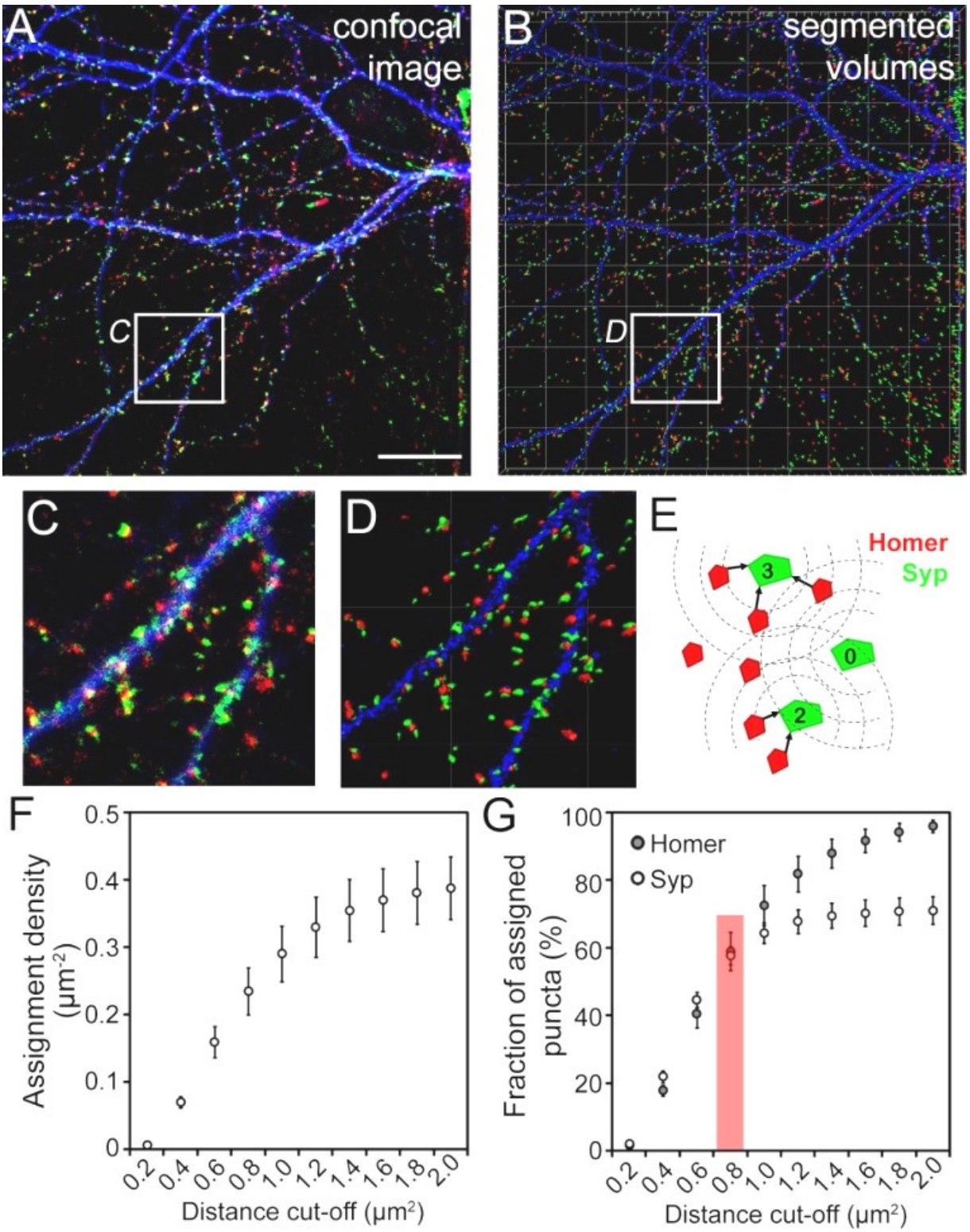


**Figure S1.** Synapse analysis workflow and the determination of the distance cut-off. **A.** An exemplary dendrite in the synaptic chamber. Image shows the maximum intensity projection of Homer 1 (red), Synaptophysin 1 (green), and MAP2 (blue) stains. **B.** Segmentation of the same image in Imaris. **C-D.** Marked areas in *A* and *B*, respectively, magnified 3.5×. **E.** Principle of assigning postsynaptic (Homer) to presynaptic (Syp) puncta based on proximity. Numbers indicate the number of assignments for each presynaptic puncta. **F.** Synaptic assignment density as a function of distance cut-off. **G.** Fractions of assigned pre- and postsynaptic puncta as a function of distance cut-off, showing that Syp assignments saturate at around 1.0 µm for the dataset analyzed. N = 9 microfluidic devices from 4 independent cultures; 5-8 images per device. Bars show SEM.

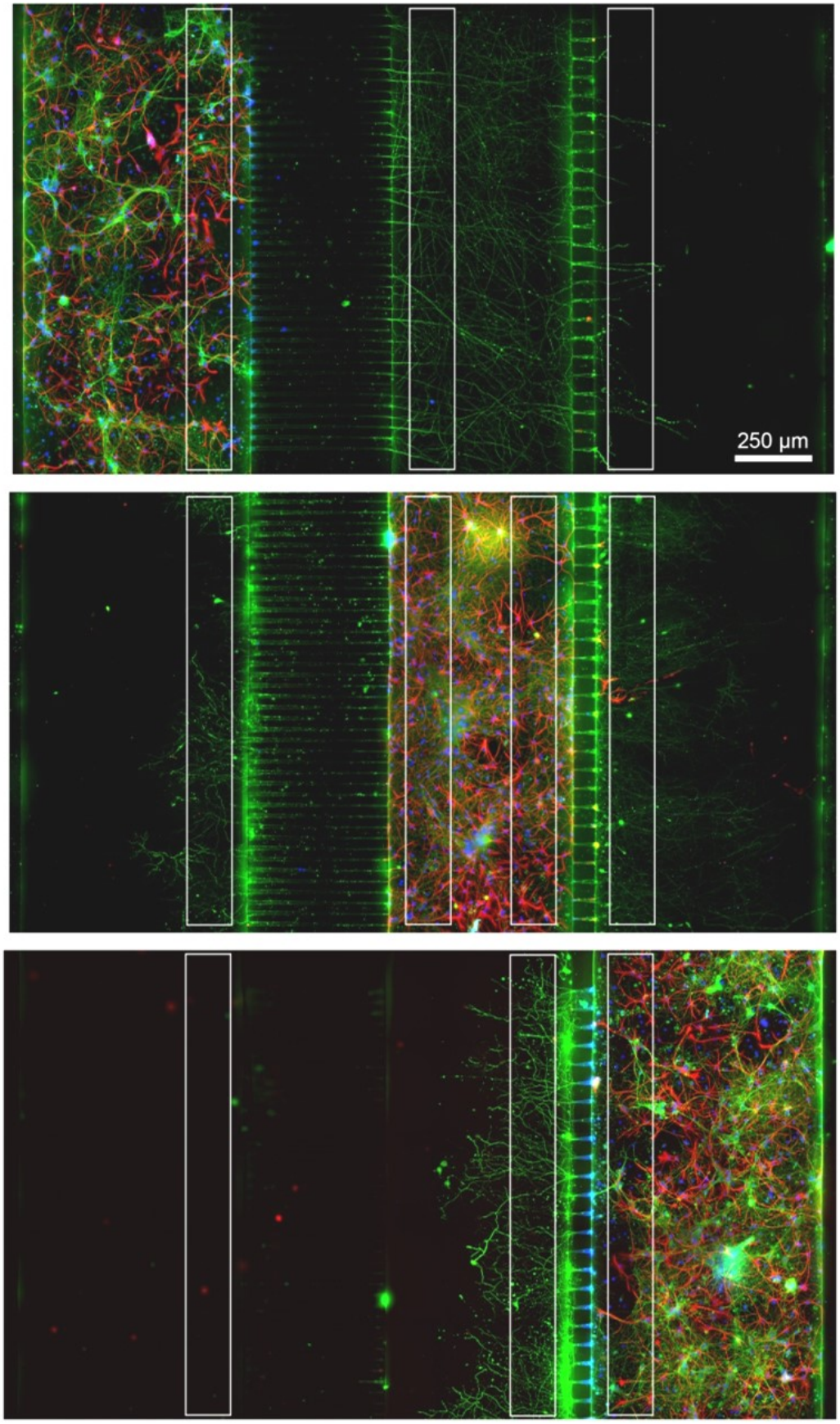


**Figure S2.** Exemplary images of microfluidic devices where primary neurons were plated in only one chamber. β3-tubulin (green), Hoechst (blue), and GFAP (red) staining at DIV14. White rectangles indicate regions where β3-tubulin staining intensity was measured to calculate penetration ratios.

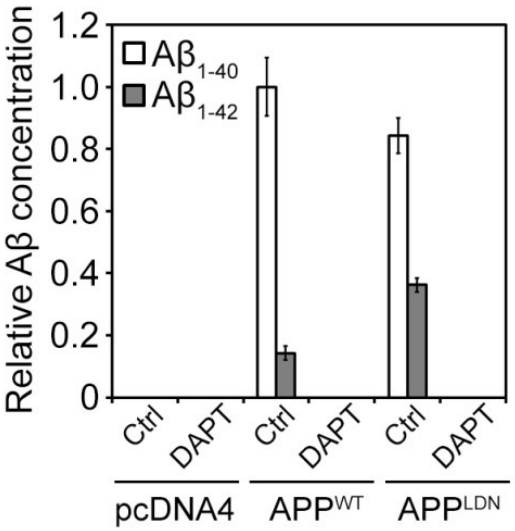


**Figure S3.** Relative $A\beta_{1-42}$ concentration in off-chip CHO cell media quantified via ELISA. γ-secretase inhibitor DAPT was applied at 18 µg/mL for 5 d. Data normalized to $APP^{WT}$ control condition. As the sample was concentrated prior to $A\beta_{1-42}$ measurement, $A\beta_{1-42}$ levels cannot be directly compared to $A\beta_{1-40}$ levels.

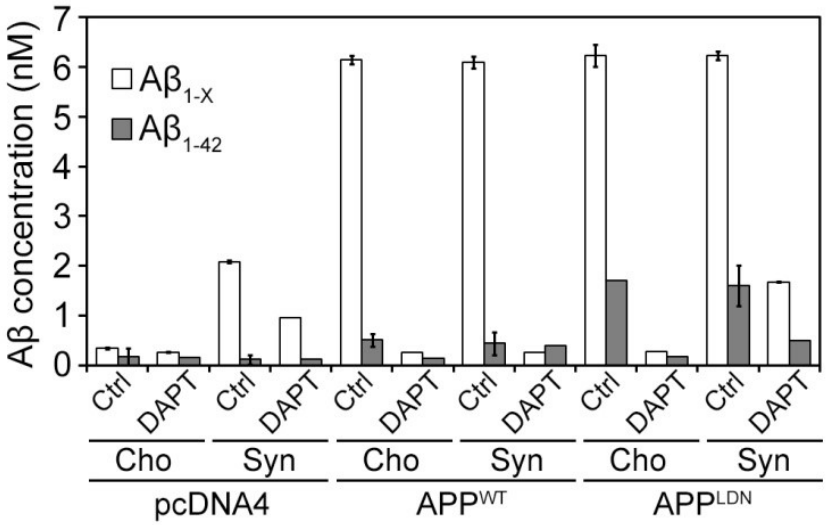


**Figure S4.** Concentration of $A\beta_{1-X}$ and $A\beta_{1-42}$ in the media collected from different reservoirs of the co-culture device at DIV14 measured via Alpha-LISA. Cho: Co-culture chamber; Syn: Synaptic chamber. Note that data for the synaptic chamber are identical to what is shown in Figure 2D.

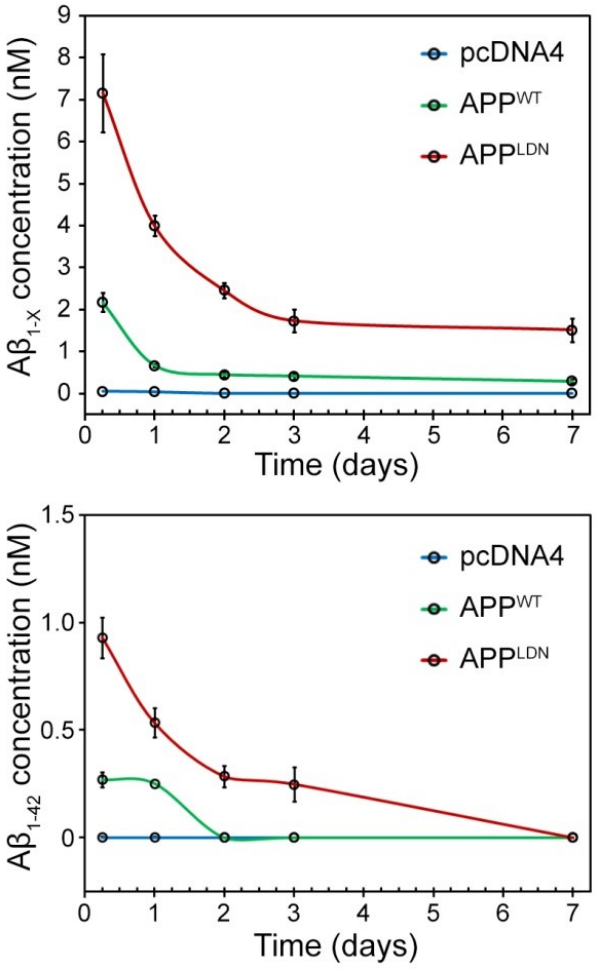


**Figure S5.** Concentration of $A\beta_{1\text{-}X}$ and $A\beta_{1\text{-}42}$ in the media collected from primary neurons cultured in 384-well plates and exposed to CHO cell-conditioned media for 6 h to 7 d. Concentration was determined *via* Alpha-LISA using 6-8 wells per condition. Error bars indicate standard deviation of the mean.

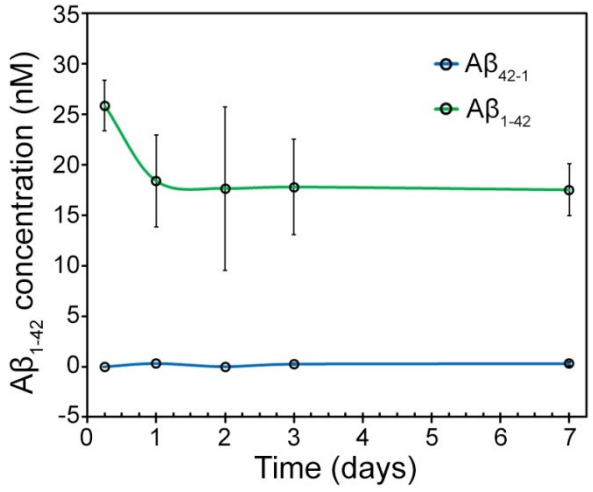


**Figure S6.** Concentration of $A\beta_{1\text{-}42}$ in the media collected from primary neurons cultured in 384-well plates and treated with synthetic $A\beta_{1\text{-}42}$ oligomers for 6 h to 7 d. Concentration was determined *via* Alpha-LISA using 6-8 wells per condition. Error bars indicate standard deviation of the mean.

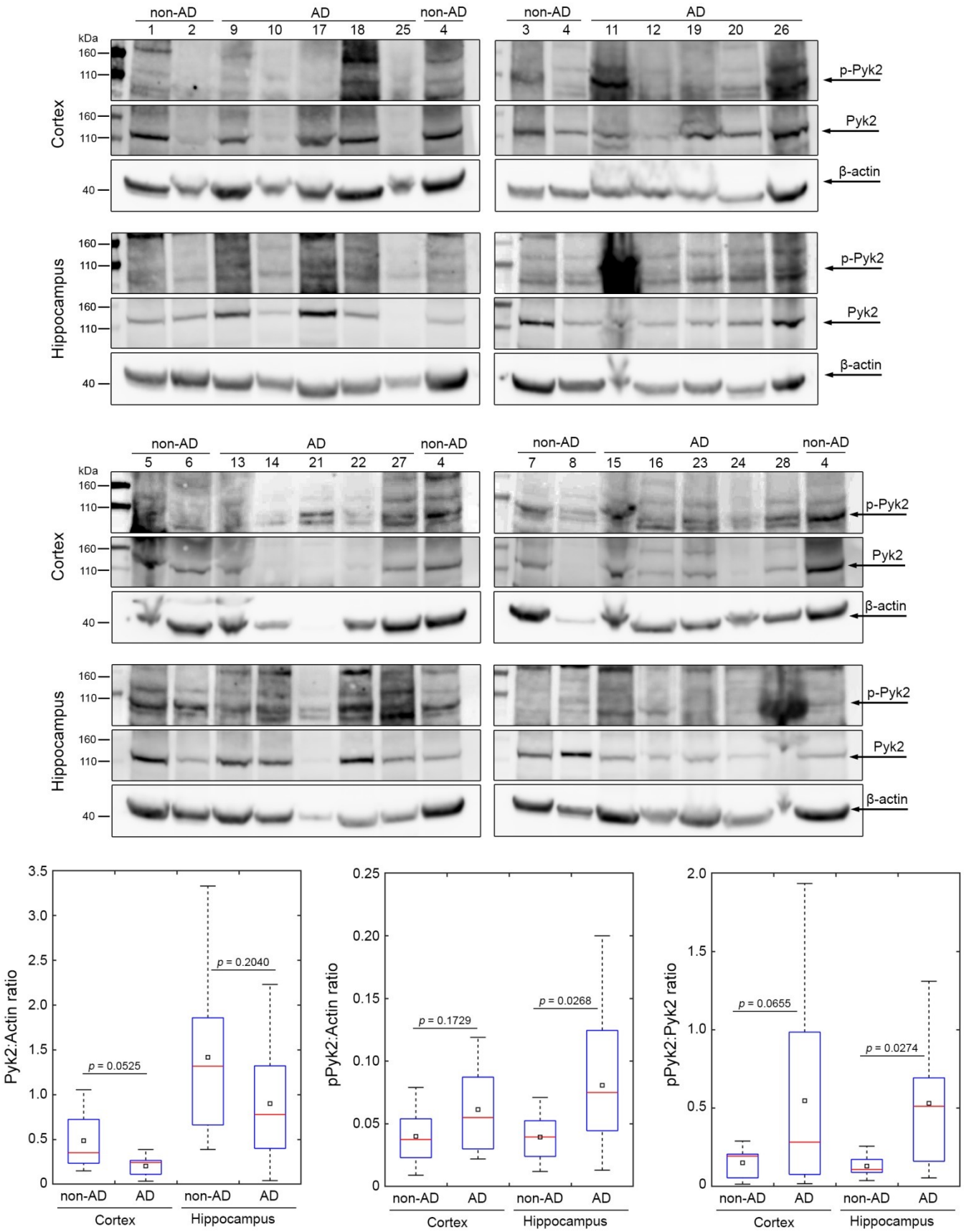


**Figure S7.** Total and phospho-Pyk2 levels in the post-mortem brains of AD cases and healthy controls. Demographic details of the cohort are given in Table S1. In box plots, red bars and black squares indicate sample median and mean, respectively. Wilcoxon rank-sum test; * $p < 0.05$; ** $p < 0.01$; *** $p < 0.005$; N/S: not significant.

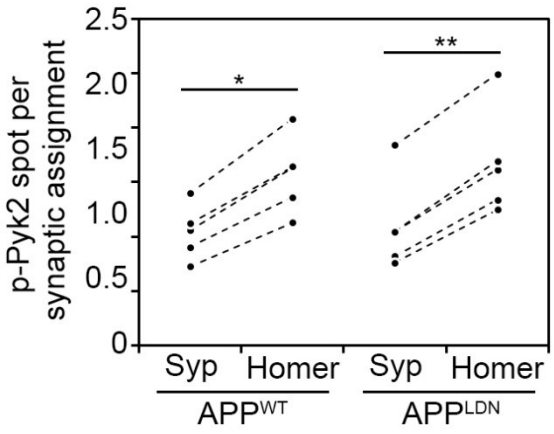


**Figure S8.** Localization of phospho-Pyk2 Tyr402 (p-Pyk2) puncta relative to synapses. Each Homer spot was assigned to the nearest Synaptophysin (Syp) spot within cut-off distance of 1.0 µm. Each p-Pyk2 spot was assigned to the nearest "synapse", *i.e.*, to the midpoint between Syp and Homer spots, within cut-off distance of 1.5 µm. Such assignments were then categorized as presynaptic or postsynaptic, if they were inside of 45° cones emanating from the midpoint towards Syp and Homer spots, respectively. N = 5 devices per condition from 2 independent experiments. * $p < 5\times10^{-4}$; ** $p < 5\times10^{-5}$; paired t-test.

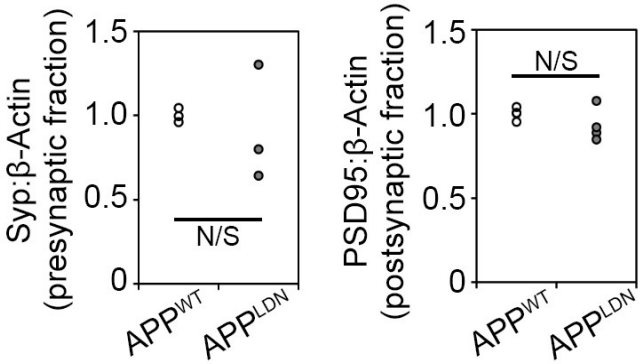


**Figure S9.** Quantification of synaptic markers in the synaptosomal fraction. Synaptophysin (Syp) in the presynaptic fraction and PSD95 in the postsynaptic fraction for primary neuronal cultures exposed to media collected from CHO-APP$^{WT}$ and CHO-APP$^{LDN}$ cultures. N/S: not significant.

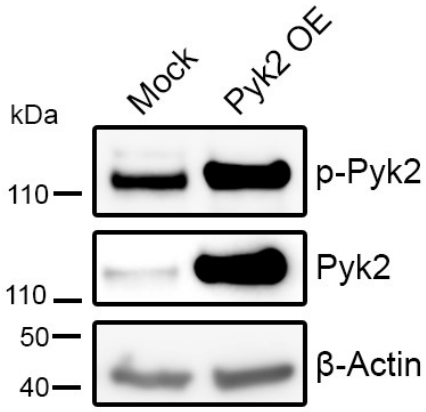


**Figure S10.** An exemplary immunoblot demonstrating the overexpression of Pyk2 in primary neuronal cultures at DIV14 following lentiviral transduction at DIV7.

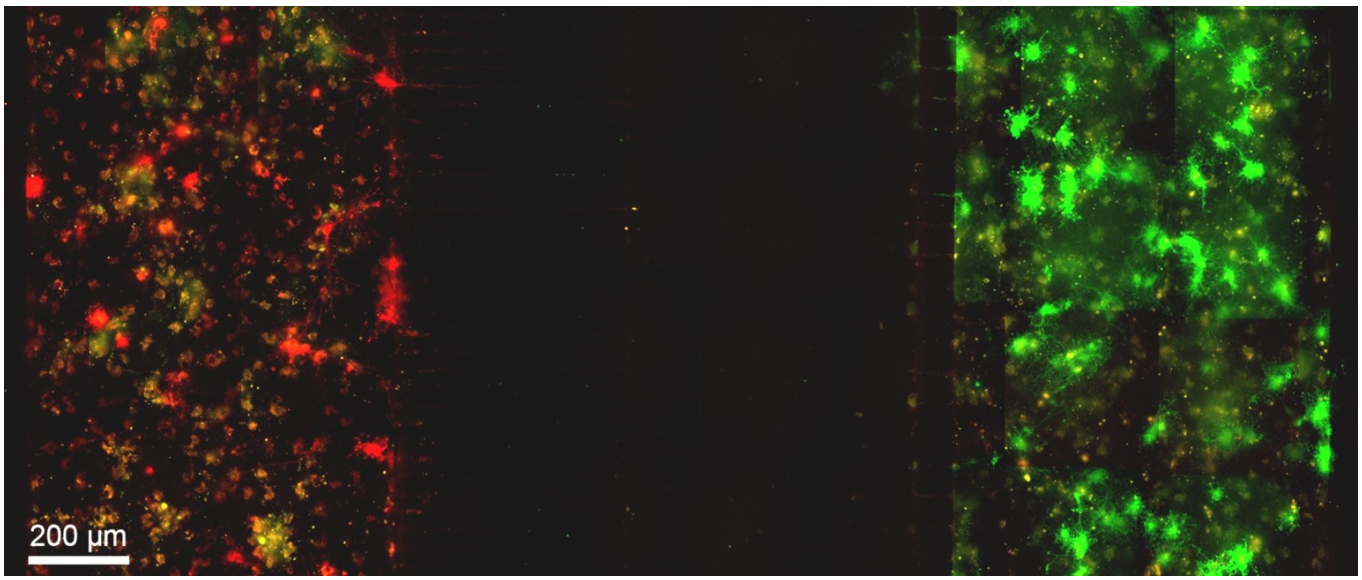


**Figure S11.** Demonstration of isolated lentiviral treatments at DIV14. Cells cultured in pre- and postsynaptic chambers were transducted at DIV7 with lentiviruses to express LifeAct-ruby (red) and LifeAct-GFP (green), respectively.